Chapter 7

Tempering Resistance

7.1 Introduction

It was demonstrated in the last chapter that the weld metal designed using the neural network models and the general principles of physical metallurgy achieved the properties demanded by industry. The material is intended primarily for use in the welding of boiler components in large power plant. As such, the service temperature is likely to be in the range 500–600 °C. The weld metal is therefore likely to temper during service. It would be interesting therefore to examine experimentally the tempering resistance of the new weld metal and to compare it with HCM2S tube steel.

At the same time, two further experimental welds were made for this work, using the manual metal arc welding process at ESAB AB (Sweden). Neither both of these contained vanadium or niobium as deliberate additions, but were conceived to reveal the effect of substituting tungsten for molybdenum in a classical $2\frac{1}{4}$Cr–1Mo weld metal. They also contained a low carbon concentration consistent with the HCM2S philosophy.

The compositions of the three alloys and the new weld metal discussed in Chapter 6 are listed in Table 7.1. It is worth noting that the atomic concentration of tungsten in the Cr–W alloy is almost identical to the atomic concentration of molybdenum in the Cr–Mo alloy, the atomic weight of tungsten is much higher than that of molybdenum.

Phase diagram calculations were carried out using MTDATA [124] with the SGTE Steels database to reveal the equilibrium precipitates to be expected at 500 and 600 °C. MTDATA works by accessing thermodynamic data from the SGTE database in order to use solution models and minimise the free energy of the system to find the equilibrium states. In all cases, the calculations allowed for the existence of Laves phase, chromium carbides, vanadium carbides, α-ferrite, M_3C, M_7C_3, M_6C, $M_{23}C_6$, MC phases and the following components: Fe, C, Mn, Si, Cr, Mn, Mo, Ni, N, Nb, V, W and Ti.

The results are listed in Table 7.2, but more details will be presented during the discussion of

the experimental data. It is evident at this stage that there are significant differences between the equilibrium states of the four alloys and when the two tempering temperatures are compared. These results will be compared against actual tempering experiments later in this Chapter. Because of the time taken in designing the new weld metal, it was not possible to study its tempering behaviour for 500 °C.

	C	Si	Mn	P	S	Ni	Cr	Mo	W	V	Nb	B	N
HCM2S	0.060	0.20	0.47	0.006	0.002	0.10	2.27	0.09	1.50	0.23	0.05	0.004	0.008
Cr–W	0.073	0.38	0.74	0.011	0.011	0.04	2.11	0.01	1.99	0.016	-	-	0.02
Cr–Mo	0.068	0.38	0.74	0.010	0.011	0.06	2.11	0.93	0.01	0.021	-	-	0.02
New WM	0.057	0.32	0.67	0.010	0.007	0.10	2.10	0.2	0.63	0.20	$\leq$ 0.02	$\leq$0.002	0.015

Table 7.1: Chemical composition (in wt%) of HCM2S steel [119, 117] and low–alloy Cr–Mo, Cr–W weld metals and designed new weld metal (New WM).

	500 °C	**600** °C
Cr–Mo Weld metal	$M_{23}C_6$, VN, Cr_2N	$M_{23}C_6$, Cr_2N
Cr–W Weld metal	$M_{23}C_6$, M_6C, Cr_2N	M_7C_3, M_6C, Cr_2N
HCM2S Steel	M_6C, VN, (Nb,V)C	M_6C, CrNbC, V_4C_3
New weld metal	$M_{23}C_6$, M_6C, V(C,N), CrNbC	M_7C_3, $M_{23}C_6$, M_6C, CrVTiN

Table 7.2: Calculated equilibrium precipitates, calculated using MTDATA [124].

7.2 Experimental Procedure

Various experimental techniques were employed to understand and evaluate the tempering resistance of these alloys.

7.2.1 Heat Treatment

The HCM2S was received in the form of tubes which had been heat treated at 1050 °C for 1 h followed by air cooling to generate a bainitic microstructure, which was in turn tempered at 770 °C for 1 h. This is the standard commercial heat–treatment prior to service. The weld metals were all produced using the manual metal arc welding process with 4 mm diameter electrodes, as "bead–on–plate" deposits on mild steel plate. Each deposit was 4 cm thick and consisted of seven layers so that dilution effects essentially disappeared after the first layer. All samples were machined avoiding the first layer. For heat–treatment purposes, the samples were machined as $8 \times 8 \times 10$ mm square–sectioned rods, which were then sealed in quartz tubes filled with a partial pressure of argon. To ensure a consistent starting microstructure, each sample,

irrespective of alloy type, was heated to 1100 °C for 10 min; the sealed sample was then quenched in water whilst breaking the quartz tubes. The samples were then sealed again in quartz tubes for prolonged tempering at either 500 or 600 °C. The heat–treatment procedure is illustrated in Fig. 7.1.

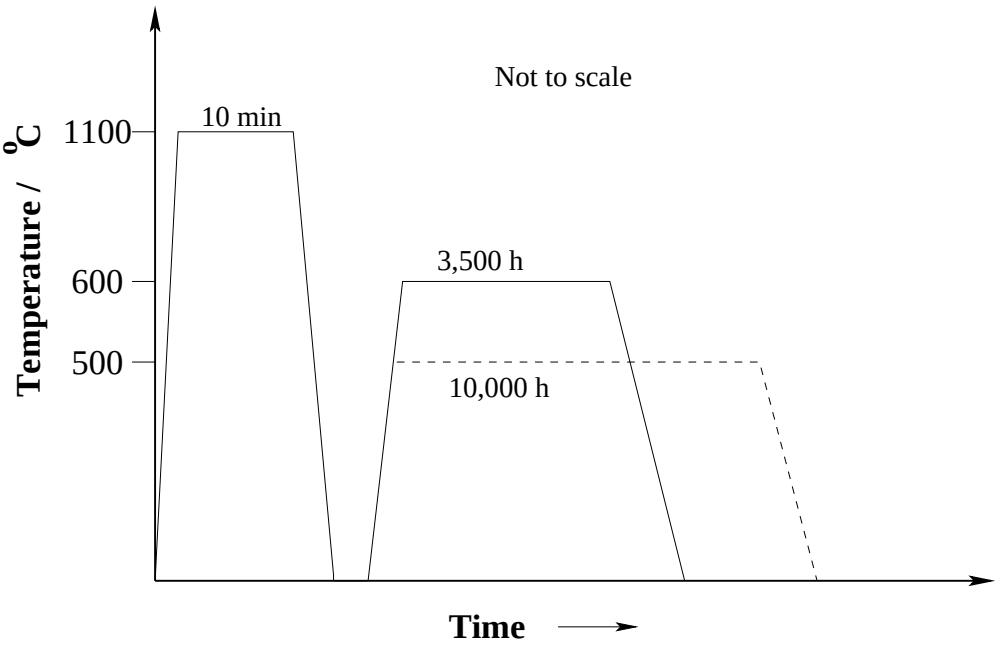

Figure 7.1: The heat treatment cycle followed in the present work.

7.2.2 Hardness Measurements

A Vickers hardness testing machine with 10 kg load and $\frac{2}{3}''$ objective was used to measure the macrohardness of the steel samples. The load was applied for 15 seconds during testing. Ten measurements were taken diagonally covering the whole sample surface. The samples were mounted on conductive Bakelite, then ground to 600 grit paper before testing.

7.2.3 Optical Microscopy

All samples were prepared for microstructural examination by hot mounting in conductive Bakelite powder, followed by grinding upto 1200 grit, then diamond polished to 1 μm. A 2% nital etchant(2% concentrated nitric acid in methanol solution) was used to etch the samples.

7.2.4 Scanning Electron Microscopy

A JEOL JSM 820 scanning electron microscope (SEM) was used to view the etched samples prepared as described in Section 7.2.3.

7.2.5 Transmission Electron Microscopy

For transmission electron microscopy (TEM) examination, thin foil and extraction carbon replicas were used.

Camera Constant

A TEM consists of electromagnetic lenses which amongst other things control the magnification of the diffraction patterns. The magnification of diffraction patterns in a TEM is expressed as a camera length, as shown in Fig. 7.2.
The camera constant is expressed as;

$$Rd_{hkl} = L\lambda = \text{Camera constant} \tag{7.1}$$

where R is the real distance between the transmitted spot and the diffracted spot, L is the camera length, d_{hkl} is the spacing of the $\{hkl\}$ crystallographic planes and λ is calculated using the following equation:

$$\lambda = \frac{h}{\sqrt{2meV(1 + \frac{eV}{2mc^2})}} \qquad (\text{Å}) \tag{7.2}$$

where h is Plank's constant, m and e are the electron mass and charge respectively, V is the accelerating voltage of the electrons and c is the speed of light in vacuum.

The camera constant was measured by examination of the diffraction pattern from sputtered gold on a copper grid at 200 kV on JEOL 200CX TEM. For a given electron beam direction a number of particles are oriented so as to satisfy the Bragg equation [132] hence each plane gives a number of reflections lying in a cone of angle 4θ. The final diffraction pattern contains a number of concentric rings corresponding to the $\{hkl\}$ planes which are diffracting, Fig 7.3.

To calculate the camera constant the diameters of the rings in the diffraction pattern were measured, then the ratio of the squares of the radii of the outer rings to those of the first or second low–index ring were calculated. This enables the N values corresponding to each of the rings to be found using equation 7.3.

$$N^2 = h^2 + k^2 + l^2 \tag{7.3}$$

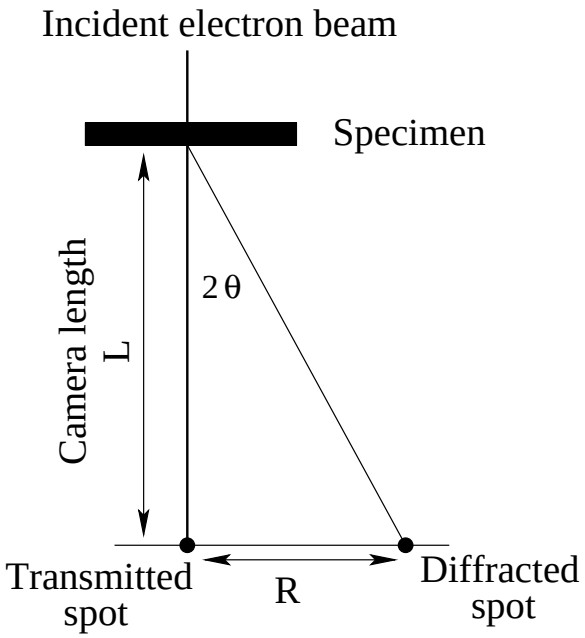

Figure 7.2: Schematic diagram showing the magnification of a diffraction pattern by electron microscopic lenses.

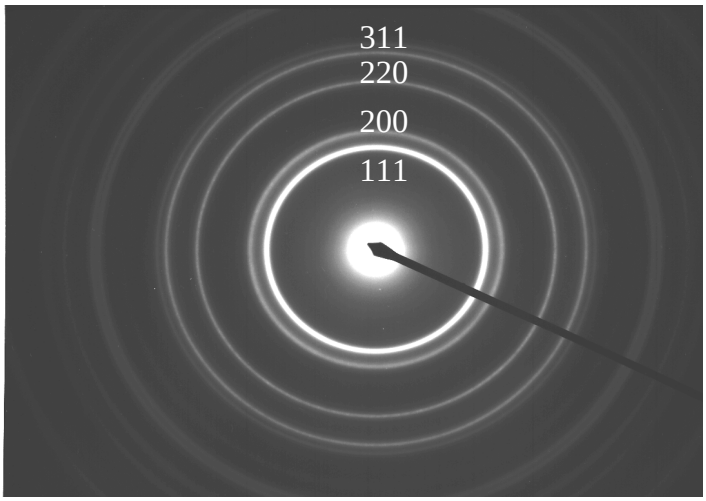

Figure 7.3: Diffraction pattern from the sputtered gold film used to determine the camera constant at 137 cm camera length (L) and 200 kV.

where *h, k and l* are the plane indices. Then *d*–spacings were calculated using equation 7.4 for cubic systems.

$$d = \frac{a}{\sqrt{N}} \tag{7.4}$$

The accurate lattice parameter (a) of gold is 4.0780 Å [133] and the calculated d–spacings are shown in Table 7.3. The calculated camera constants at different camera lengths at 200 kV are shown in Table 7.4.

Precipitates were identified using selected area electron diffraction. Convergent beam electron diffraction technique was used for very small particles.

Ring	Lattice spacing (d) in Å
1	2.355
2	2.039
3	1.442
4	1.230
5	1.177
6	1.096
7	0.935
8	0.912
9	0.832

Table 7.3: The calculated d–spacing in gold.

Camera length / cm	Calculated camera constant / 10^{-12} m^2
82	2.00
137	3.36
205	5.18

Table 7.4: Calculated camera constants for a number of different camera lengths at electron accelerating voltage of 200 kV.

Thin Foils

Thin samples were sliced using a high–speed SiC cutting wheel and 3 mm diameter discs were punched from these slices. The discs were ground to 50 μm by hand on 1000 grit paper. The thinned discs were then electropolished using a twin–jet electropolisher at 45 V. The electropolishing solution used was 5% perchloric acid, 20% glycerol in alcohol. A JEOL 200CX transmission electron microscope was used to examine thin foils.

Carbon Replicas

Carbon replicas can be more useful than thin foils in the identification of precipitates. Carbon replicas eliminate magnetic effects due to the ferrite matrix and enable a large area to be examined. The procedure followed to extract the replicas from surfaces prepared using optical microscopy is shown in Fig. 7.4. Carbon was deposited in a vacuum of 10^{-5} torr on to the etched sample. Then the deposited carbon layer on the sample surface was cut into 2 mm square pieces to enable the removal of several small sections covering the whole area of the sample. Then the film was detached from the sample by electrolytic etching in a solution 5% hydrochloric acid in methanol at 1.5 volts. Each replica was washed in methanol and then in distilled water. Finally the floating replicas in distilled water were collected on 400 square mesh copper grids for examination in the transmission electron microscope.

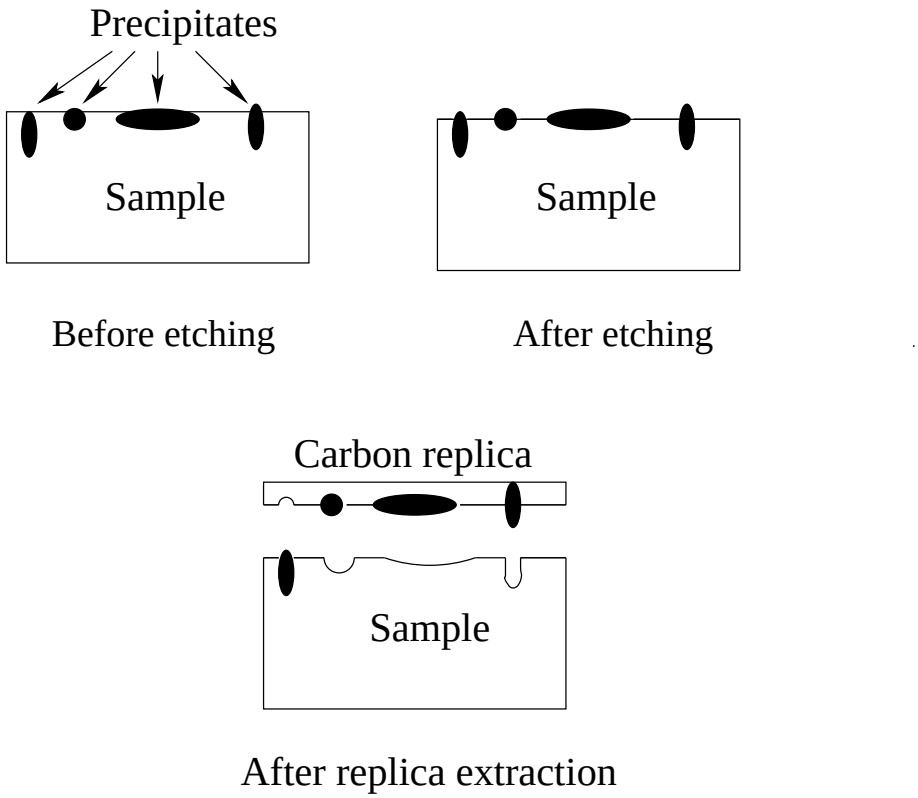

Figure 7.4: Schematic diagram illustrating the preparation of carbon replicas.

7.2.6 Analysis of Electron Diffraction Patterns

An electron diffraction pattern is essentially a planar section of the reciprocal lattice, each reciprocal lattice vector lying along the normal to a plane and of magnitude equal to the inverse

of the interplanar spacing. Thus, the distance of each diffracted spot from the central beam is inversely proportional to the spacing of the planes that it represents. The angle between a pair of reciprocal lattice vectors represents the angle between the normals to those planes. The geometry of the electron diffraction pattern in a transmission electron microscope is illustrated in Fig. 7.2.

As can be seen from the list of crystal structures presented in Table 7.5, many of the structures are not cubic and are complicated in detail. This makes it quite difficult to interpret the patterns, since plane normals and directions with the same indices are then not necessarily parallel. The problem can be ameliorated by using a computer program [134, 135] which deals with the analysis of the patterns for any crystal structure. Data from the diffraction pattern are fed into the program, together with an estimate of measurement accuracy and a trial crystal structure. The program then searches the reciprocal space to find zone axes which are consistent with the pattern. However, the number of trial crystal structures is very large in the present work. Therefore, a new modified program was created, so that it is no longer necessary to input a trial structure, but instead, a list of possible trial structures is read by the program. The program then searches through the entire set to find matches with the experimental data. This proved vital because many of the electron diffraction patterns were found to be ambiguous with respect to the precipitate phase. In those circumstances, it was found that the intensities of the diffraction spots could be compared with standard X–ray tables to reduce or eliminate ambiguities. Intensities, take into account the structure factor which the computer program described above does not (it only has systematic absences, such as those differentiating the primitive cubic and body–centered cubic lattices). Information about the computer programs is presented in Section B.3.

7.2.7 X–ray Diffraction

Bulk precipitates were extracted from bulk samples by electrolyticaly dissolving the matrix in 5% hydrochloric acid in methanol solution at 1.5 V. The specimen was made the anode and platinum the cathode. After 5–6 h the anodic sample dissolved in the electrolyte, leaving the precipitates which were filtered on filter paper containing 1 μ pores, washing throughly during filtration with methanol. X–ray diffraction of the extracted particles was used for the identification of various precipitates formed during tempering. A Siemens D500 diffractometer (CuK_α target) was used to scan between 20° and 140° θ at a step size of 0.04° for 10 seconds. The diffraction peak positions were located using Phillips Analytical software, which was also used to calculate the associated intensities of the peaks. X–ray diffraction was used as verification of the precipitates identified using electron diffraction analysis.

Precipitate	Crystallographic system	Lattice parameter(s) in Å	Reference
M_3C	Orthorhombic	a=4.525, b=5.087, c=6.743	[116]
M_7C_3	Orthorhombic	a=4.526, b=7.01, c=12.142	[116]
M_2C	Hexagonal	a=2.888, c=4.559	31–0403 [136]
M_6C	Cubic	a=11.082	[116]
$M_{23}C_6$	Cubic	a=10.621	[116]
NbC	Cubic	a=4.4702	10–181 [136]
Nb_4N_3	Tetragonal	a=4.382, c=8.632	20–0803 [136]
VN	Cubic	a=4.09	25–1252 [136]
VC	Cubic	a=4.3	74–1220 [136]
V_4C_3	Cubic	a=4.16	1–1159 [136]
WC	Hexagonal	a=2.9062, c=2.83	25–1047 [136]
W_2C	Hexagonal	a=2.99, c=4.72	2–1134 [136]
CrNbN	Tetragonal	a=3.037, c=7.391	25–0591 [136]

Table 7.5: The crystallographic data used to identify the selected precipitates in electron diffraction pattern. Numbers in reference column indicate X–ray data card number.

7.3 Comparison of Cr–W and Cr–Mo Weld Deposits

The hardness data from tempering experiments at 500 °C, for time periods up to 11,000 h, are presented in Fig. 7.5, along with hardness curves obtained using neural network models fitted with the experimental data in Fig. 7.6 and 7.7. Both alloys show a significant resistance to tempering when compared with a plain carbon steel of the same carbon concentration, Fig. 7.5. This must be due to secondary hardening. Secondary hardening is associated with the formation of carbides during tempering of water quenched material containing strong carbide forming elements such as Cr,V, Mo, Nb, etc.

The initial and final hardnesses are not very different in these materials, but the peak hardness attained is important. Transmission electron microscopy and electron diffraction revealed that a key difference between the alloys is the presence of M_2X in the Cr–Mo alloy, Fig. 7.13. Some electron diffraction patterns and TEM micrographs are provided in Figs 7.8 to 7.16. In molybdenum–containing steels, Mo_2C is an important precipitation strengthening carbide [23]. It commonly precipitates as fine needles (Fig. 7.13) parallel to the $< 110 >_\alpha$ direction in ferrite. The orientation relationship is that of Pitsch–Schrader [137]:

$$(011)_\alpha \parallel (0001)_{M_2C},\ [100]_\alpha \parallel [11\bar{2}0]_{M_2C}$$

This Mo_2C is a key strengthening phase in Cr–Mo weld metal, and indeed, is responsible for the secondary hardening peak as illustrated in Fig 7.5. In multirun welding secondary hardening

causes an increase in the hardness in the reheated regions, which is not desirable in keeping the as–welded hardness low. Tungsten is beneficial in this respect because it does not harden the microstructure during reheating in multirun welding [138, 139]. Figs 7.6 and 7.7 illustrate the hardness variation with tempering time as measured and smoothed using neural network representation. Here the neural networks helped to visualise the trends in hardness.

The hardness of the tungsten–containing alloy begins to drop abruptly beyond about 90 h at temperature whereas that of the Cr–Mo alloy is maintained to some 256 h. The precipitates identified are tabulated in Table 7.7. To summarise, the main consequences of the substitution of tungsten for molybdenum in this class of steels are as follows:

a. M_2X precipitation only occurs in the molybdenum–containing alloy; since this is a significant strengthening precipitate, the tempering resistance of molybdenum–containing steel is expected and found to be larger.

b. Tungsten has a high solubility in M_6C; therefore, $M_6C$is an equilibrium phase in the Cr–W alloy but not in the Cr–Mo alloy, Table 7.6. Furthermore, the precipitation of $M_{23}C_6$is accelerated in the Cr–W alloy. Robson and Bhadeshia [140] have demonstrated both theoretically and experimentally that the large volume fractions of metastable M_2X and M_7C_3, which form prior to $M_{23}C_6$, deplete the matrix and therefore suppress $M_{23}C_6$ precipitation [140]. This does not happen in the Cr–W system, where $M_{23}C_6$is obtained more rapidly. $M_{23}C_6$is not very effective as a hardening precipitate in low–alloy steels [23].

c. It is interesting to note that precipitation in the Cr–W alloy effectively removes almost all the tungsten from solid solution, Table 7.6 . The main role of tungsten, in the long term, is therefore to form M_6C.

7.4 Comparison of HCM2S and New Welding Alloy

The new weld metal and HCM2S steel were subjected to austenitisation at 1100 °C, followed by water quenching and then tempered at 600 °C. The results are shown in Fig. 7.17 and TEM micrographs of HCM2S steel and the new weld metal are provided in Figs 7.19 to 7.27. The new weld metal is softer than HCM2S steel by around 50 HV. The precipitates found in these materials are shown in Table 7.8 and corresponding constituents of each equilibrium precipitate are given in Table 7.9. The softness of the new weld metal can be explained that the HCM2S steel contains V_4C_3 as a thermodynamically stable precipitate, whereas it is a metastable precipitate in the new weld metal. In addition, HCM2S has the CrNb nitride. Furthermore, HCM2S has a higher tungsten content. Fine precipitates were found in HCM2S steel (Fig. 7.19a) after 4 h and 3,500 h (Fig. 7.21) of tempering, whereas in the new weld metal coarse precipitates were

	Cr-W weld metal			Cr-Mo weld metal		HCM2S steel		
Total number of moles	1784.0			1801.0		1783.0		
	Cr_2N	$M_{23}C_6$	M_6C	Cr_2N	$M_{23}C_6$	(Nb,V)C	VN	M_6C
Amount in moles	4.37	12.1	**24.72**	3.4	27.3	2.65	1.8	**20.28**
Element (mole fraction)								
Fe	0.001	0.15	0.45	0.001	0.169	0.0	0.0	0.38
C	0.11	0.21	0.14	0.003	0.21	0.27	0.015	0.14
Cr	0.58	0.56	0.006	0.60	0.52	0.001	0.085	0.006
Mn	0.007	0.082	0.0	0.011	0.0	0.0	0.001	0.0
N	0.32	0.0	0.0	0.33	0.0	0.0	0.32	0.0
W	0.015	0.0	**0.40**	0.0	0.0	0.01	0.001	**0.35**
Mo	0.0	0.0	0.0	0.04	0.10	0.0	0.0	0.05
V	-	-	-	-	-	0.36	0.58	0.075
Nb	-	-	-	-	-	0.15	0.0	0.0

Table 7.6: Equilibrium mole fraction of elements in equilibrium precipitates in Cr–W, Cr–Mo weld metals and HCM2S steel at 500 °C, calculated using MTDATA [124]. In Cr–W weld metal and HCM2S steel at equilibrium, the major phase M_6C contains tungsten as a main constituent.

	66 h	128 h	10,000 h
Cr–W weld metal	M_3C, M_7C_3	-	M_7C_3, $M_{23}C_6$, M_3C
Cr–Mo weld metal	-	M_3C, M_7C_3, M_2C	M_7C_3, M_3C, M_2C

Table 7.7: The precipitates identified in Cr–W and Cr–Mo weld metals during tempering at 500 °C upto 10,000 h.

found (Fig. 7.25) after 3,500 h of tempering. However, in practice the HCM2S steel is heavily tempered (780 °C for 1 h) prior to service, so that its as–received hardness is about 200 HV and its yield strength is 400 MPa. The designed weld metal self tempers during service and matches the hardness of HCM2S steel base plate. The new weld metal hardness is comparable with that of normalised and tempered HCM2S steel, Fig. 7.18. Moreover the service temperature of this designed new weld metal is much lower than 600 °C.

7.5 Comparison of HCM2S and Cr–W Weld

HCM2S is much more resistant to tempering than the straight Cr–W alloy purely because of vanadium and niobium carbonitrides. This was found during the comparative study of HCM2S steel and Cr–W weld metal. In HCM2S steel after 960 h of tempering, the precipitates CrNbN, M_3C, V_4C_3 and M_7C_3 were found. The presence of CrNbN (Fig. 7.32) was verified with X–ray

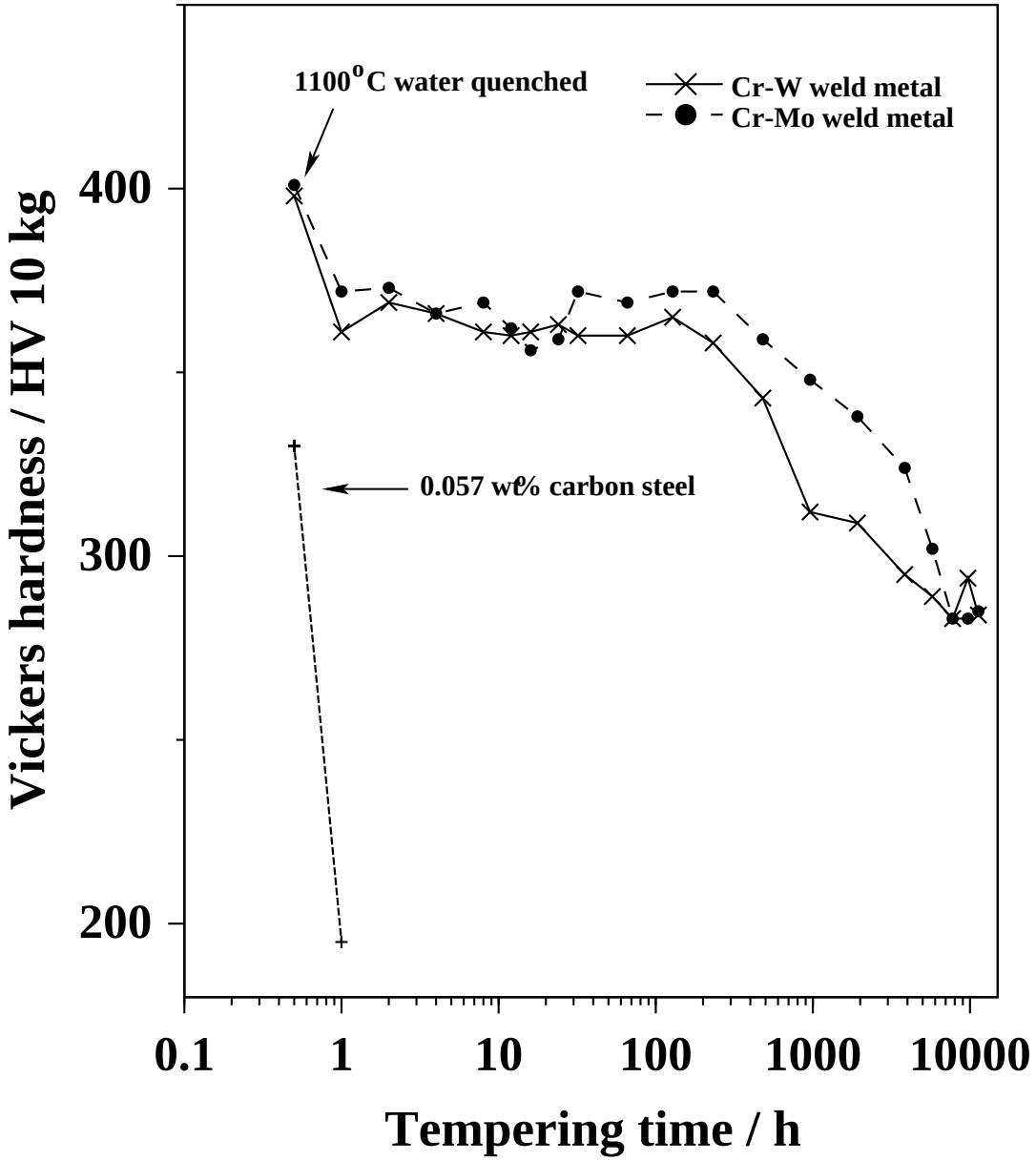

Figure 7.5: The change in hardness in Cr–Mo and Cr–W weld metals tempered at 500 °C. Data for a plain carbon steel [20] are shown for comparison.

diffraction on extracted bulk precipitates. The electron diffraction patterns and TEM micrographs are presented in Fig. 7.31 to 7.34. HCM2S steel is more stable than Cr–W weld metal (Fig. 7.28) the hardness remaining constant (Fig. 7.29). In Cr–W weld metal the major equilibrium phase is M_6C which is a coarse carbide which decreases the amount of tungsten in solid solution thus reducing the solid solution strengthening. The coarse precipitate M_6C is an ineffective precipitation strengthener. In the case of HCM2S steel coarse grain boundary precipitates

	2 h	4 h	3,500 h
HCM2S steel	-	M_3C, M_7C_3, CrNbN	M_7C_3, W_2C, V_4C_3, VC, M_3C
New weld metal	M_3C, M_7C_3	-	M_7C_3, W_2C, V_4C_3, VC, WC

Table 7.8: Precipitates identified in HCM2S steel and new weld metal during tempering at 600 °C upto 3,500 h.

	HCM2S steel			New weld metal			
Total number of moles	1783.0			1796.0			
	V_4C_3	CrNbC	M_6C	CrVTiN	M_7C_3	$M_{23}C_6$	M_6C
Amount in moles	3.95	1.552	16.61	4.286	2.75	15.6	4.73
Element (mole fraction)							
Fe	0.0012	0.001	0.41	0.005	0.096	0.26	0.42
C	0.321	0.33	0.143	0.0001	0.3	0.2	0.014
Cr	0.002	0.21	0.01	0.11	0.525	0.45	0.011
Mn	0.007	0.00	0.0	0.002	0.016	0.0	0.0
N	0.144	0.0	0.0	0.33	0.0	0.0	0.0
W	0.002	0.075	0.35	0.002	0.0025	0.02	0.34
Mo	0.0	0.036	0.037	0.0	0.0	0.064	0.038
V	0.53	0.085	0.055	0.45	0.06	0.00	0.05
Nb	0.0	0.26	0.0	-	-	-	-
Ti	-	-	-	0.1	0.0	0.0	0.0

Table 7.9: Equilibrium mole fraction of elements in equilibrium precipitates in HCM2S steel and new weld metal at 600 °C, calculated using MTDATA [124].

and fine precipitates with the grains were found (Fig. 7.30); the fine precipitates are vanadium and niobium carbonitrides which are major contributors to the strength of HCM2S steel.

7.6 Hardness of HCM2S in different conditions

Welding will induce a heat–affected zone in the HCM2S steel in the vicinity of the fusion boundary. The microstructures expected in the HAZ are essentially mixtures of bainite and martensite in different proportions. These will then temper during service. The purpose of the work presented here was to see if there are any significant differences in the tempering behaviour. Samples austenitised and water–quenched (*i.e.* martensitic) were therefore compared against an austenitised and air–cooled bainitic microstructure. Fig. 7.35 shows that, as expected, the samples start off with different hardness values, the martensitic sample being some 100 HV harder because the carbon is in solid solution. The difference in hardness decreases as the tempering

time is increased until it vanishes at about 3500 h of tempering at 600 °C. Therefore, the HAZ should become mechanically homogeneous during service. It is worth noting that the difference in hardness persists to long tempering times, much longer than expected simply from the removal of carbon from solid solution. Unfortunately, the reason for this could not be investigated due to time limitations, but it is likely that the precipitation of alloy carbides may have been altered as a function of starting microstructure. For example, it is expected that precipitation from supersaturated martensite must be finer with greater number densities of particles, whereas with a bainitic starting microstructure the cementite particles generated during the bainite transformation are known to be coarser [116].

7.7 Theoretical Analysis of Coarsening Resistance

Particle coarsening is the process of dissolution of small precipitates and the simultaneous growth of larger precipitates at a fixed volume fraction. Finally, the system should tend towards one large particle. The driving force for the process is a decrease in interfacial energy (σ) between the matrix (α) and precipitate (θ). The theory of precipitate coarsening includes the size and shape of the precipitates, the relationship between size and solubility and the mode of reaction, whether diffusion–controlled or interface–controlled [141]. A precipitate θ in a ferrite matrix α is in equilibrium when the interface is flat. When the interface becomes curved, as in spherical precipitates (Fig. 7.36) the equilibrium concentration becomes a function of the radius of curvature, given by $c_r^{\alpha\theta}$ and $c_r^{\theta\alpha}$ where $c_r^{\alpha\theta}$ is the solute concentration in the ferrite matrix and $c_r^{\theta\alpha}$ solute concentration in the precipitate θ, r is the radius of curvature of precipitate.

When the radius of curvature tends to zero, means when the curved interface becomes flat, then $c_r^{\alpha\theta} = c^{\alpha\theta}$. The solute concentration in ferrite near small particles will be greater than that near to larger particle, and it is this concentration gradient which helps the coarsening of larger precipitate at the expense of small precipitate, Fig. 7.36.

The concentration difference $c_r^{\alpha\theta} - c^{\alpha\theta}$, which drives the diffusion flux, is given by:

$$c_r^{\alpha\theta} - c^{\alpha\theta} = \frac{\sigma V^{\alpha}}{kT\, r} \times \frac{c^{\alpha\theta}(1 - c^{\alpha\theta})}{(c^{\theta\alpha} - c^{\alpha\theta})} \tag{7.5}$$

where k is the Boltzmann constant, T is the absolute temperature and V^{α} is the molar volume of ferrite matrix. Thus interfacial velocity v is proportional to the diffusion flux which in turn depends on the diffusion coefficient of solute atom in the matrix and is expressed as [142];

$$v \propto D\frac{\sigma V^{\alpha}}{kT\, r} \times \frac{c^{\alpha\theta}(1 - c^{\alpha\theta})}{(c^{\theta\alpha} - c^{\alpha\theta})^2} \tag{7.6}$$

Steels contain many solutes; each solute will influence the diffusion flux in matrix. Venugopalan *et al.* [143] suggested as effective diffusion coefficient D_{eff} by treating the fluxes as a combination of parallel electrical conductances. The interfacial velocity;

$$\frac{1}{v} \propto \frac{1}{D_i}, \qquad \text{where} \qquad \frac{1}{D_{eff}} = \sum_i \frac{1}{D_i} \times \frac{\left(c_i^{\theta\alpha} - c_i^{\alpha\theta}\right)^2}{c_i^{\alpha\theta}(1 - c_i^{\alpha\theta})} \tag{7.7}$$

where D_{eff} ($cm^2\ s^{-1}$) is the effective diffusion coefficient, D_i is the diffusion coefficient of individual solute 'i' in α–ferrite, $c_i^{\theta\alpha}$ is the solute concentration in α–ferrite and $c_i^{\alpha\theta}$ is the solute concentration of element 'i' in the precipitate (θ).

From equation 7.7; the lower the value of D_{eff} slower the growth of the precipitate. Using the above theory, D_{eff} of each precipitate for the tempered materials were calculated, Table 7.10. Here the mole faction of elements in a precipitate were calculated using MTDATA [124]. Table 7.10 shows that in the long term, well outside the scope of the experiments reported here but within the design life, it is the vanadium and niobium compounds that are the most stable and hence these will form the backbone of the creep resistance.

	D_{eff} at **500** °C	D_{eff} at **600** °C
Cr–Mo weld metal		
$M_{23}C_6$	3.15×10^{-18}	4.2×10^{-16}
Cr_2N	2.22×10^{-18}	2.74×10^{-17}
Cr–W weld metal		
M_7C_3	-	2.9×10^{-16}
$M_{23}C_6$	3.93×10^{-18}	-
M_6C	2.08×10^{-19}	2.92×10^{-17}
Cr_2N	3.01×10^{-19}	5.27×10^{-17}
HCM2S steel		
M_6C	3.4×10^{-19}	4.63×10^{-17}
V_4C_3	-	2.86×10^{-17}
VN	2.43×10^{-19}	-
(Nb, V)C	3.8×10^{-22}	-
CrNbC	-	3.0×10^{-19}
New weld metal		
M_7C_3	-	2.79×10^{-16}
$M_{23}C_6$	1.59×10^{-18}	2.38×10^{-16}
M_6C	2.85×10^{-19}	3.18×10^{-17}
V(C, N)	3.71×10^{-19}	-
CrVTiN	-	2.76×10^{-17}
CrNbC	1.0×10^{-21}	-

Table 7.10: Calculated effective diffusion coefficients ($cm^2\ s^{-1}$) for equilibrium precipitates.

7.8 Conclusions

The tempering resistance of the new welding alloy, and the changes in its hardness over a long period of time at 600 °C, have been found to be satisfactory with respect to the original design concepts. Thus, the hardness drops to about 200 HV, which is comparable to that of HCM2S when it enters service in a severely tempered state. Vanadium and niobium carbonitrides are probably vital in ensuring the long–term creep strength of both HCM2S and the new welding alloy. They form precipitates which should be more resistant to coarsening than any other precipitates found in the alloys considered. The HAZ of HCM2S should be well–behaved with respect to long periods in service in spite of the variations in major microstructural components as induced by welding. The substitution of tungsten for molybdenum keeps as-welded hardness low during multirun welding.

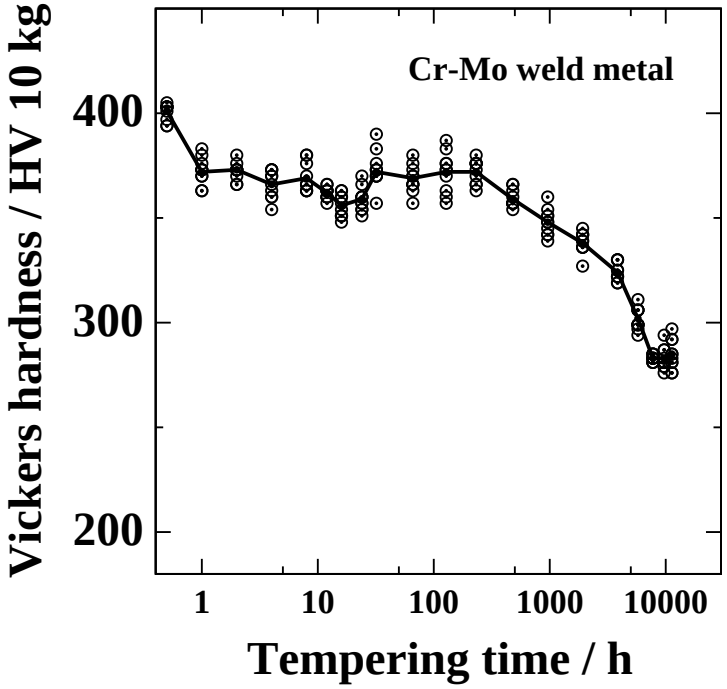

(a)

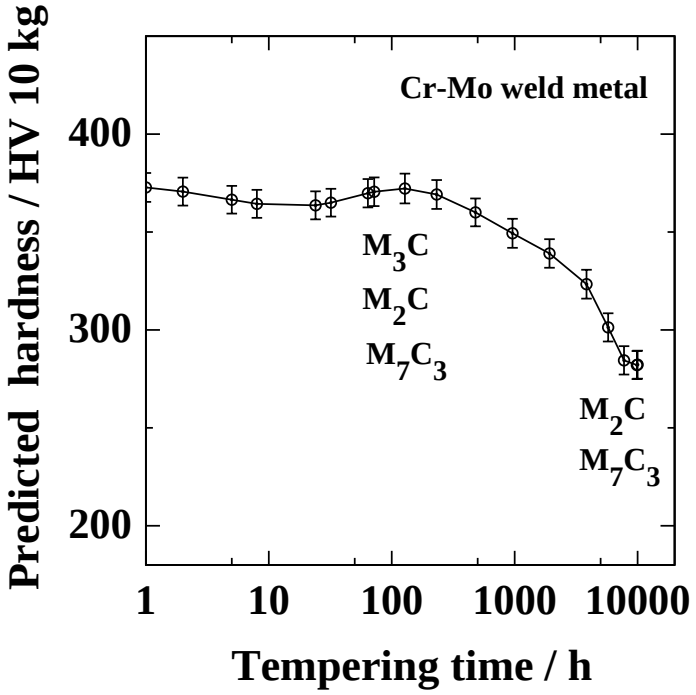

(b)

Figure 7.6: Hardness variation in Cr–Mo weld metal tempered at 500 °C, a) measured hardness, the line shows the variation in average hardness b) neural network representation of hardness data.

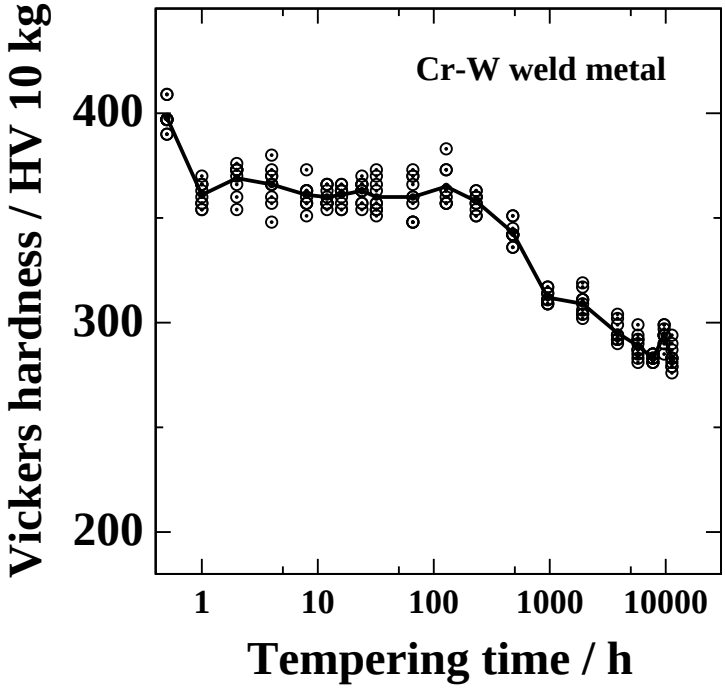

(a)

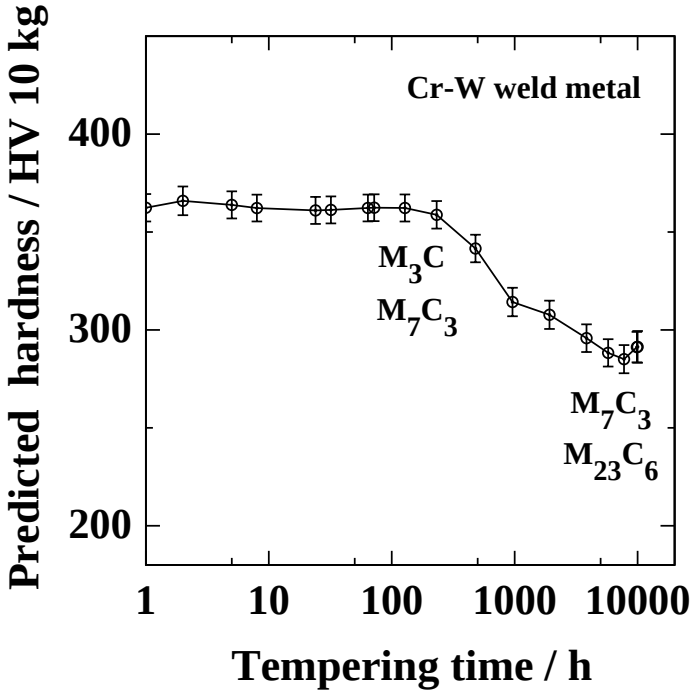

(b)

Figure 7.7: Hardness variation in Cr–W weld metal tempered at 500 °C, a) measured hardness, the line shows the variation in average hardness b) neural network representation of hardness data.

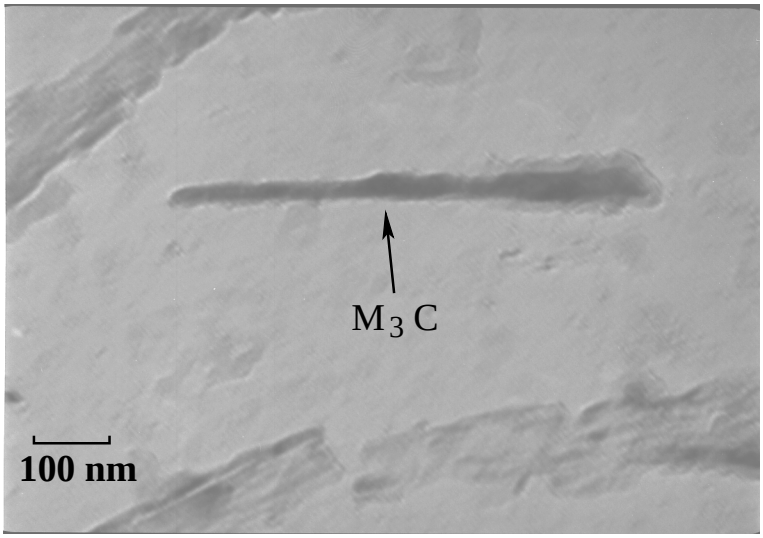

(a)

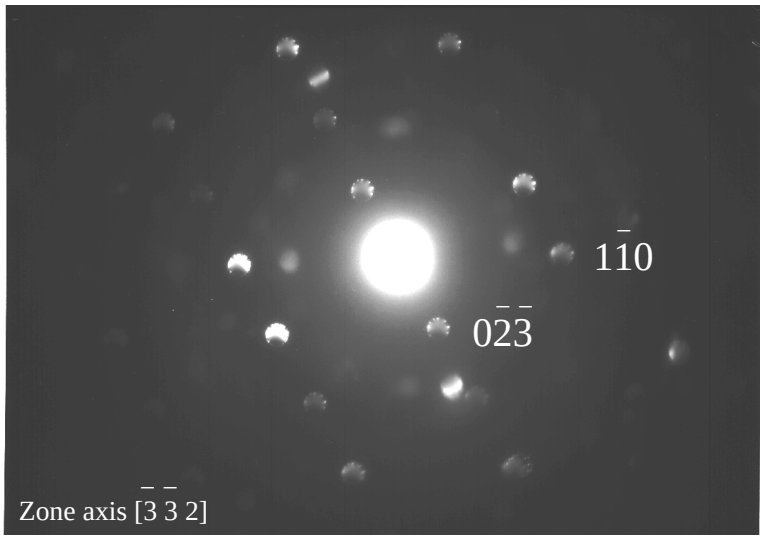

(b)

Figure 7.8: M_3C precipitate found in Cr–W weld metal tempered at 500 °C for 66 h, a) carbon replica b) electron diffraction from M_3C.

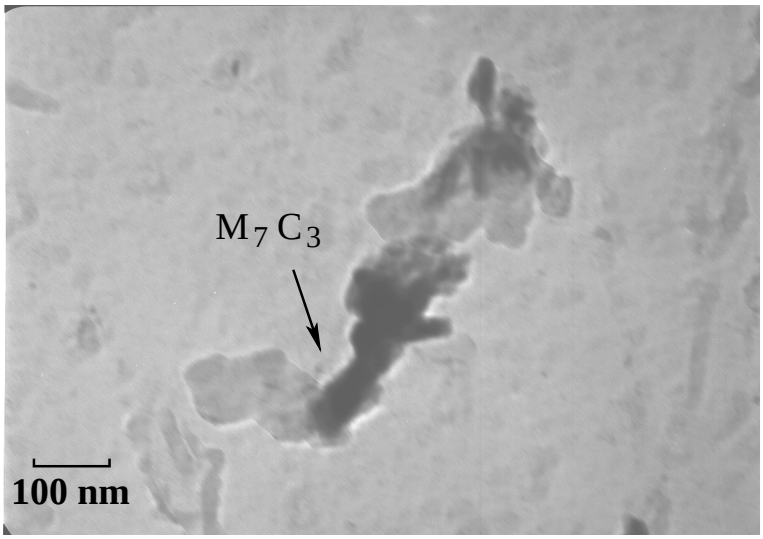

(a)

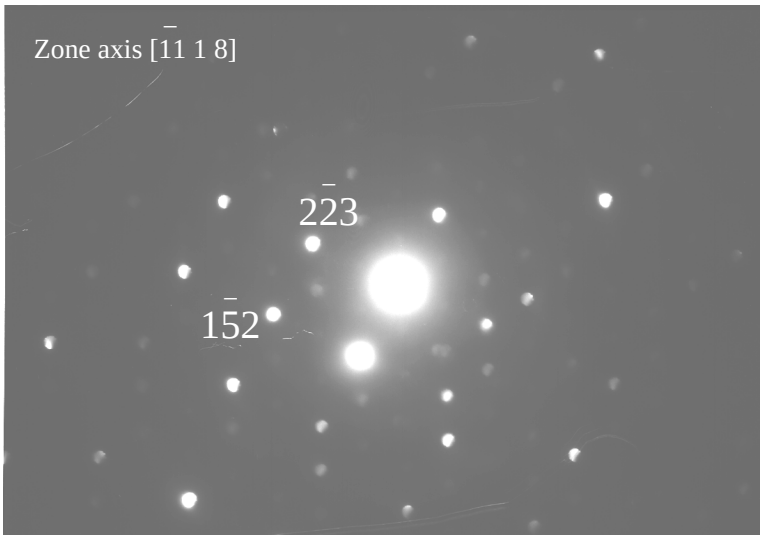

(b)

Figure 7.9: M_7C_3 precipitate found in Cr–W weld metal tempered at 500 °C for 66 h, a) carbon replica b) electron diffraction from M_7C_3.

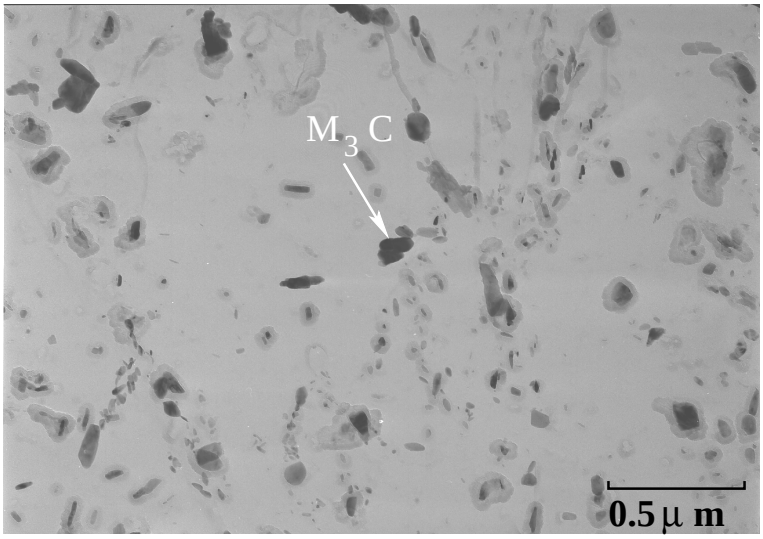

(a)

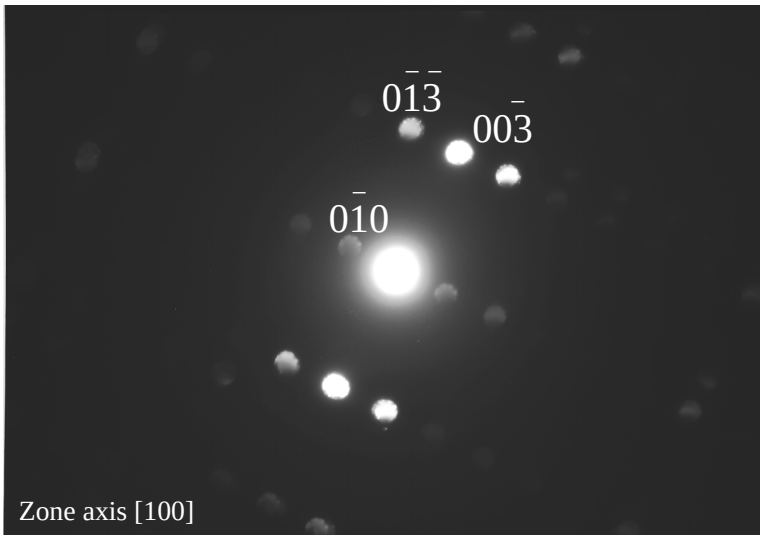

(b)

Figure 7.10: M_3C precipitate found in Cr–W weld metal tempered at 500 °C for 10,000 h, a) carbon replica b) electron diffraction from M_3C.

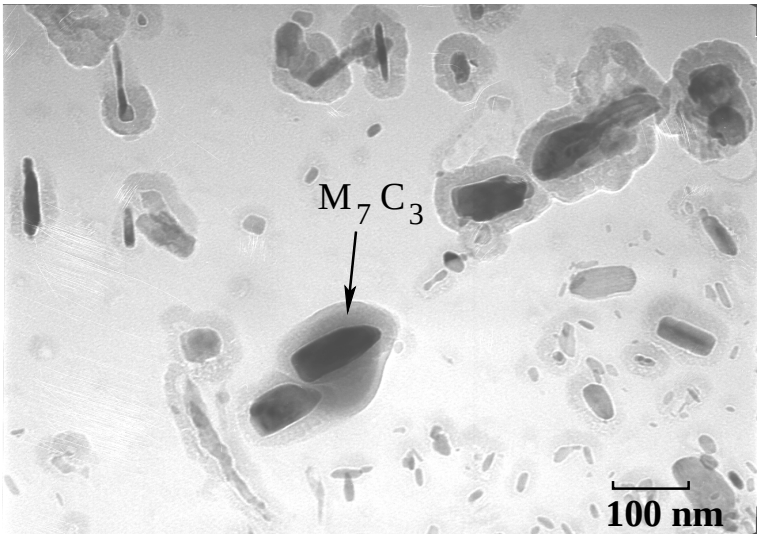

(a)

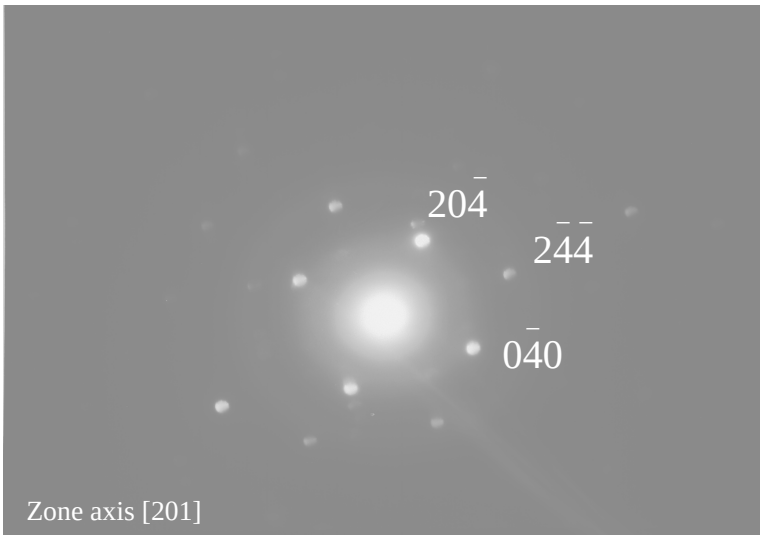

(b)

Figure 7.11: M_7C_3 precipitate found in Cr–W weld metal tempered at 500 °C for 10,000 h, a) carbon replica b) electron diffraction from M_7C_3.

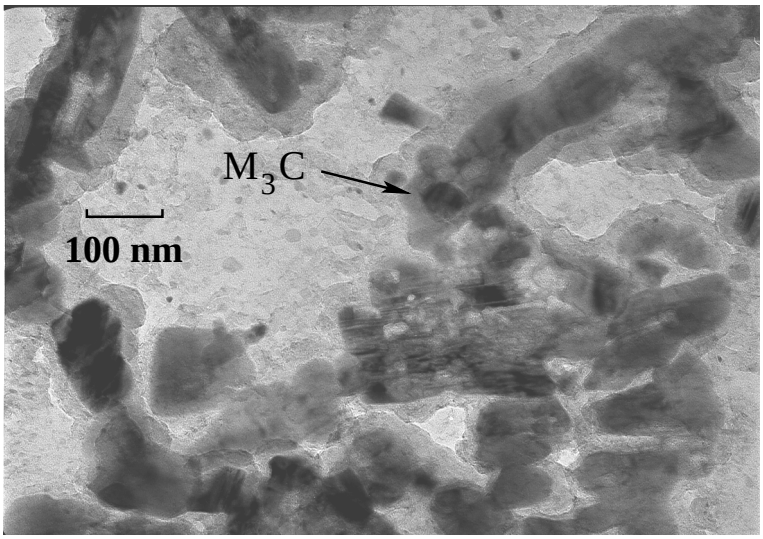

(a)

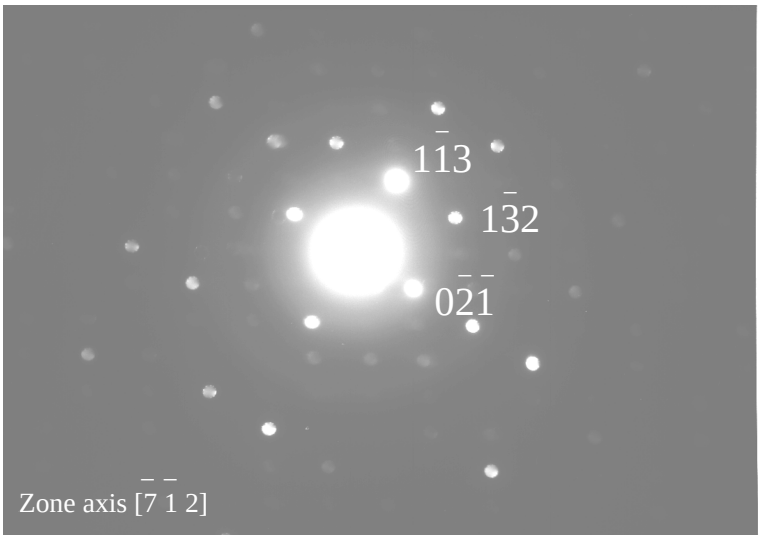

(b)

Figure 7.12: M_3C precipitate found in Cr–Mo weld metal tempered at 500 °C for 128 h, a) carbon replica b) electron diffraction from M_3C.

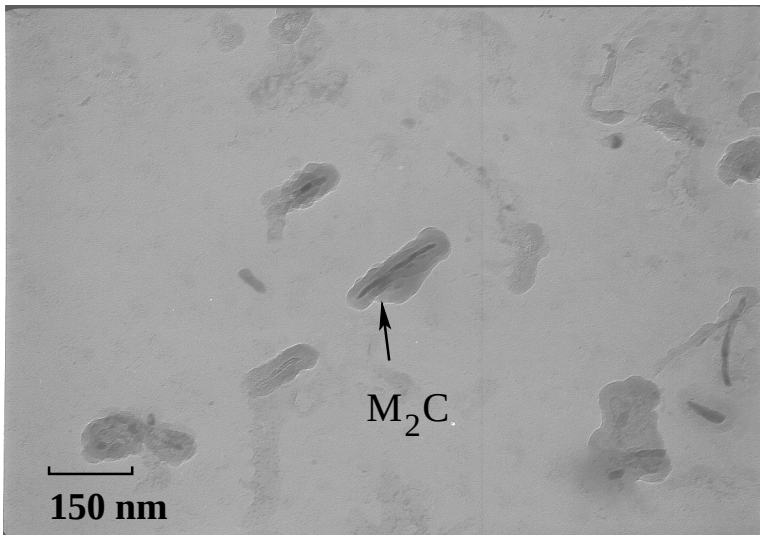

Figure 7.13: M_2C precipitate found in Cr–Mo weld metal tempered at 500 °C for 128 h, carbon replica.

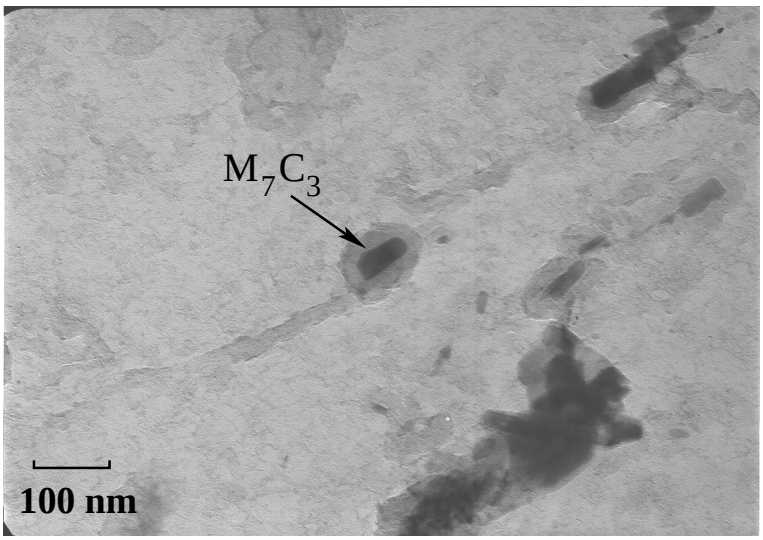

(a)

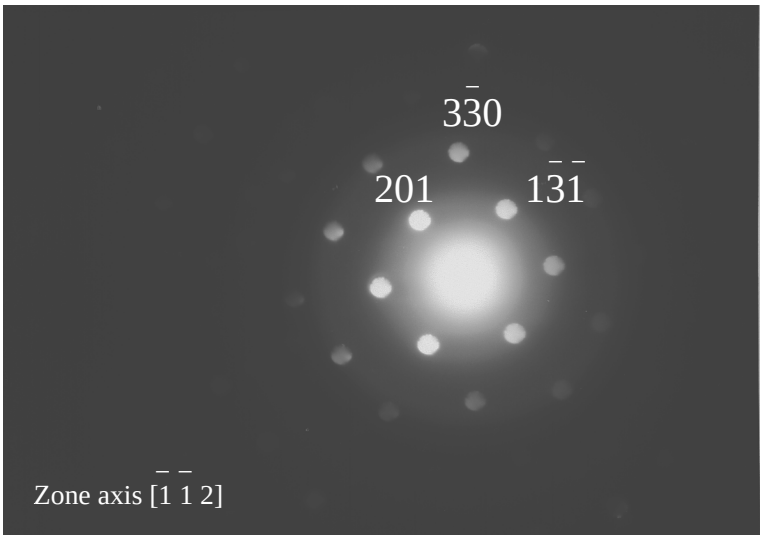

(b)

Figure 7.14: M_7C_3 precipitate found in Cr–Mo weld metal tempered at 500 °C for 10,000 h, a) carbon replica b) electron diffraction from M_7C_3.

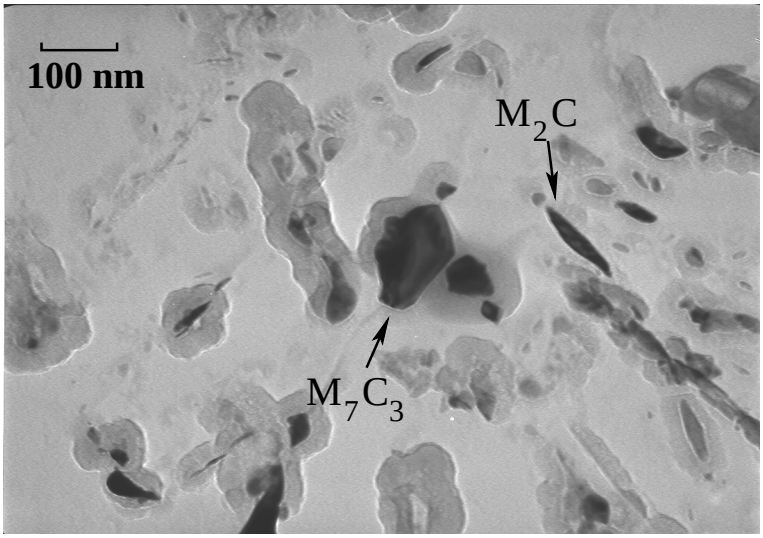

(a)

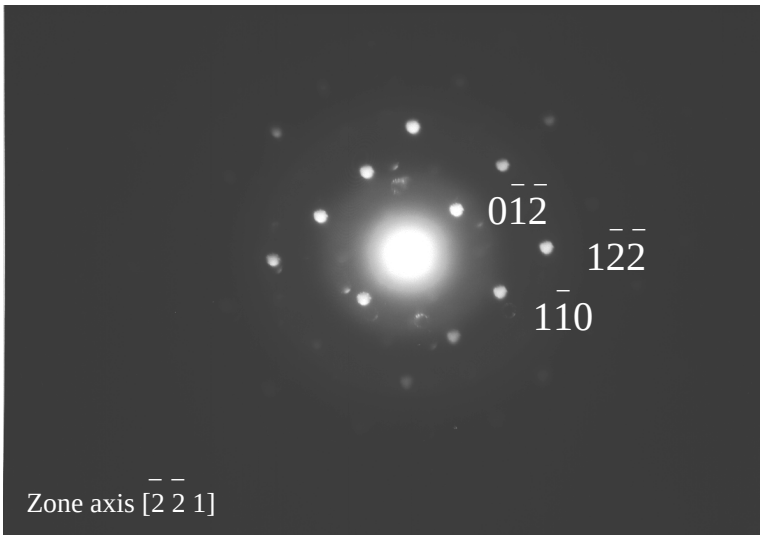

(b)

Figure 7.15: M_2C precipitate found in Cr–Mo weld metal tempered at 500 °C for 10,000 h, a) carbon replica b) electron diffraction from M_2C.

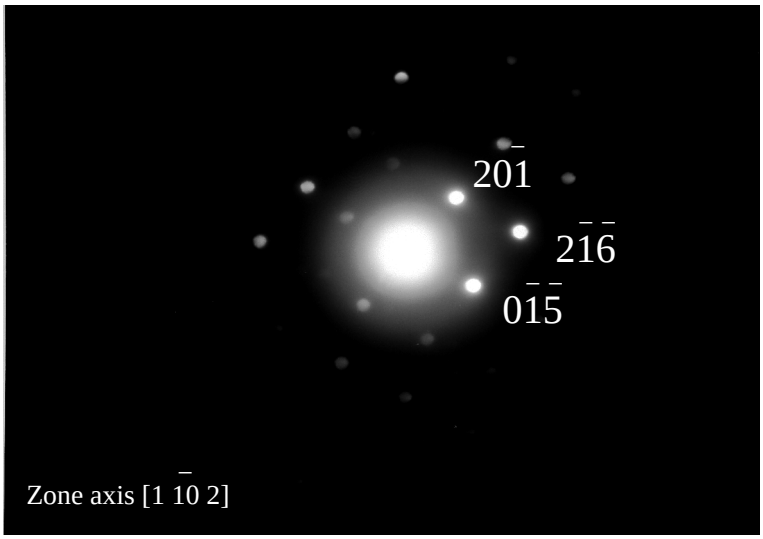

Figure 7.16: Electron diffraction pattern from the M_7C_3 precipitate found in the Cr–Mo sample, tempered at 500 °C for 10,000 h.

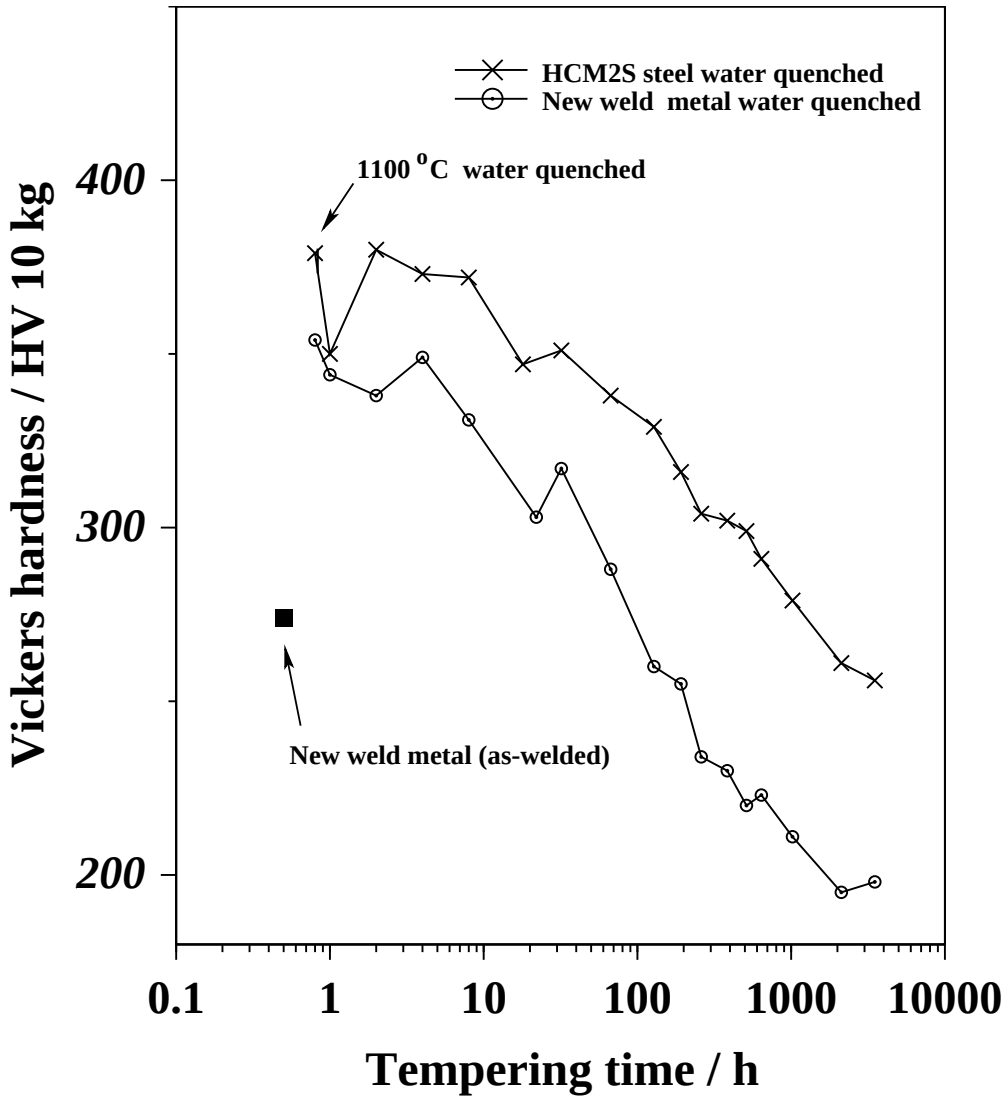

Figure 7.17: Comparison between HCM2S steel and new weld metal tempered at 600 °C.

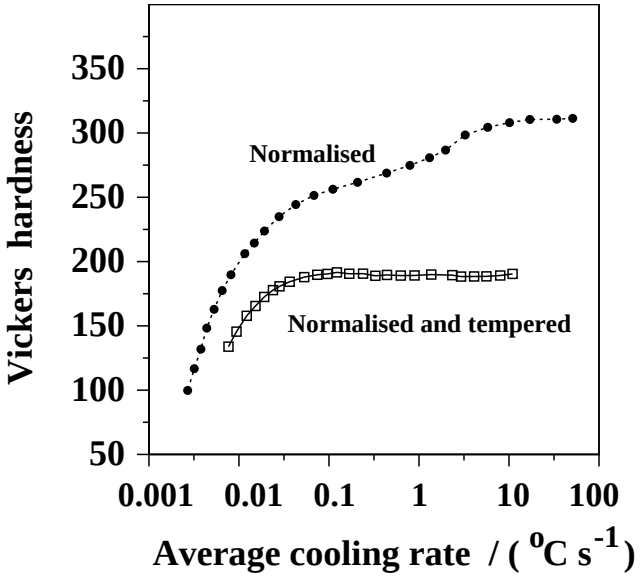

Figure 7.18: Variation in hardness of HCM2S at different cooling rates [121]. The tempering was carried at 770 °C for 1 h.

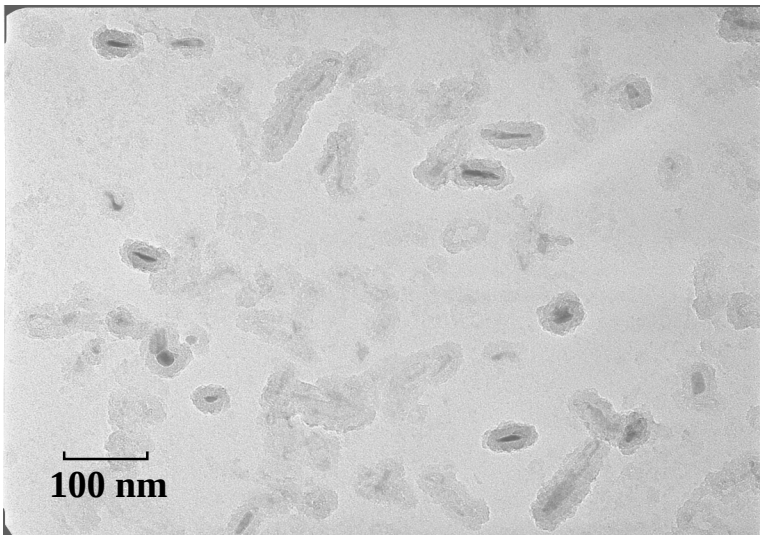

(a)

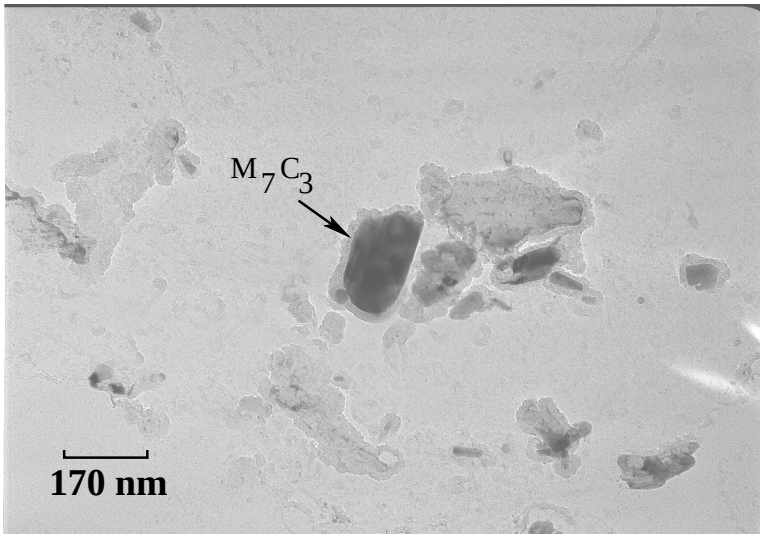

(b)

Figure 7.19: HCM2S steel tempered at 600 °C for 4 h, a) fine precipitates, carbon replica b) M_7C_3 precipitate.

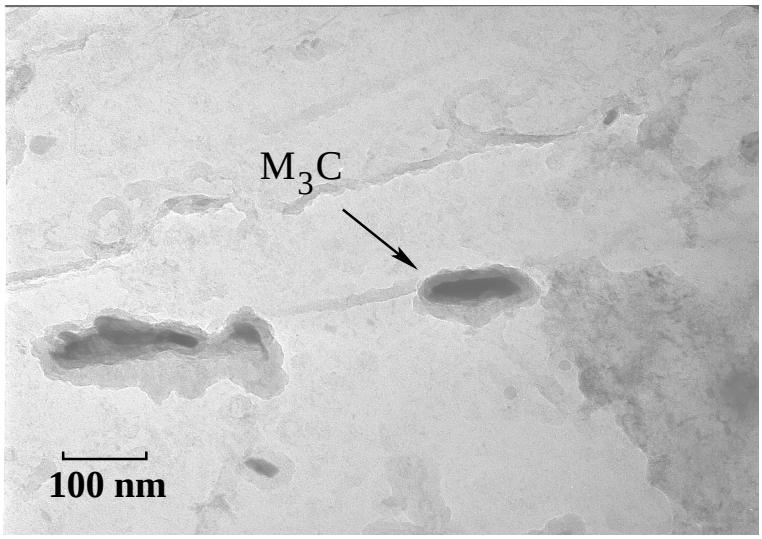

(a)

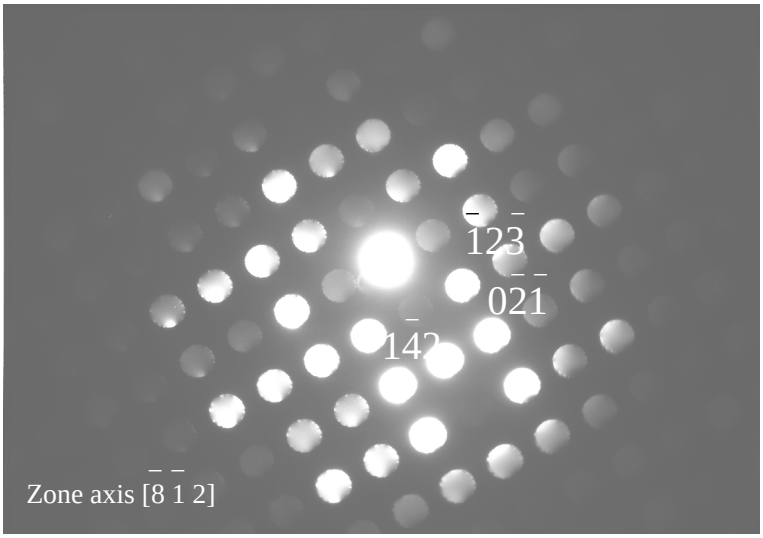

(b)

Figure 7.20: Cementite in HCM2S steel tempered at 600 °C for 4 h, a) carbon replica b) electron diffraction pattern from M_3C.

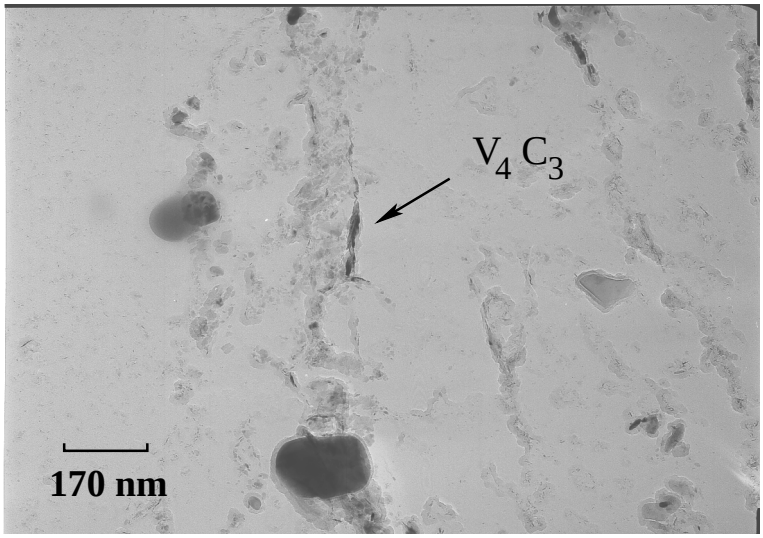

(a)

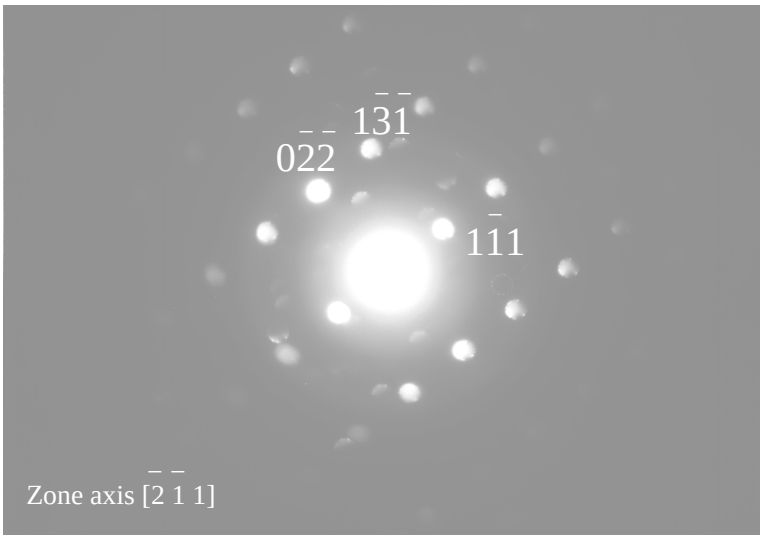

(b)

Figure 7.21: Precipitate V_4C_3 in HCM2S steel tempered at 600 °C for 3500 h, a) carbon replica b) electron diffraction from V_4C_3.

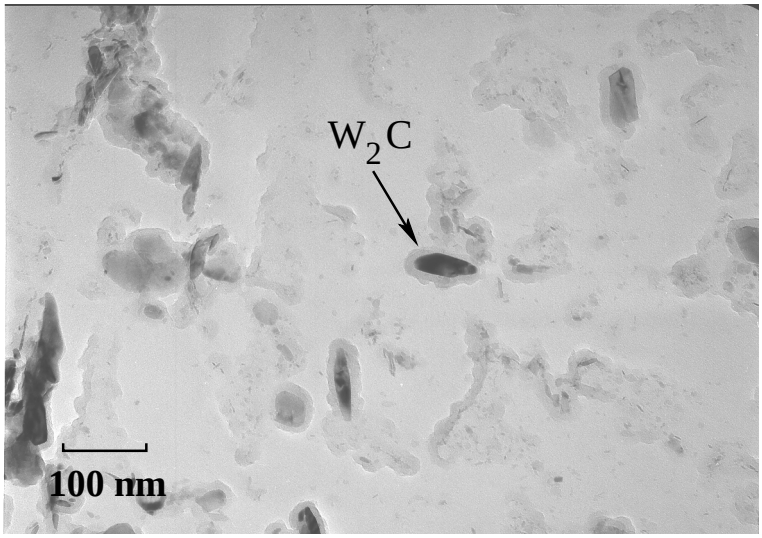

(a)

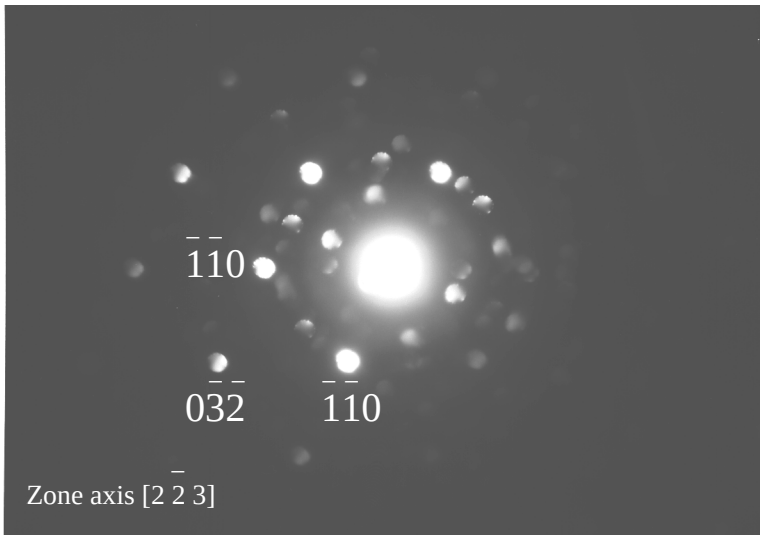

(b)

Figure 7.22: W_2C found in HCM2S steel tempered at 600 °C for 3500 h, a) electron carbon replica b) electron diffraction from W_2C.

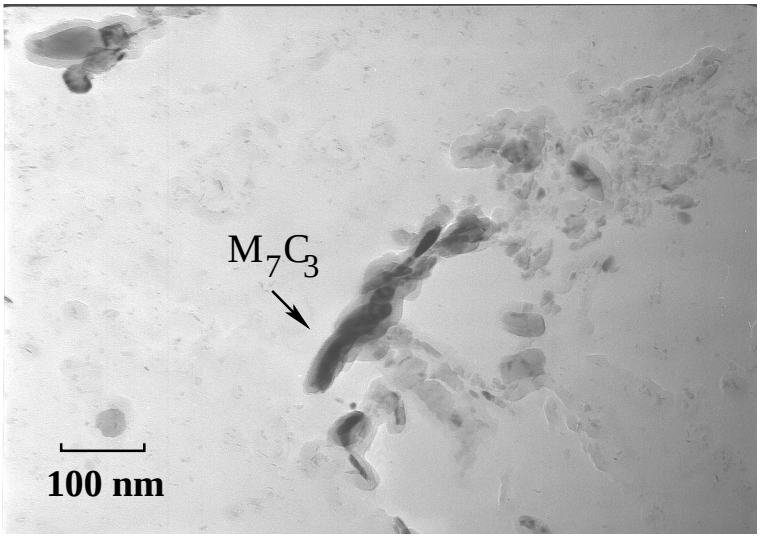

(a)

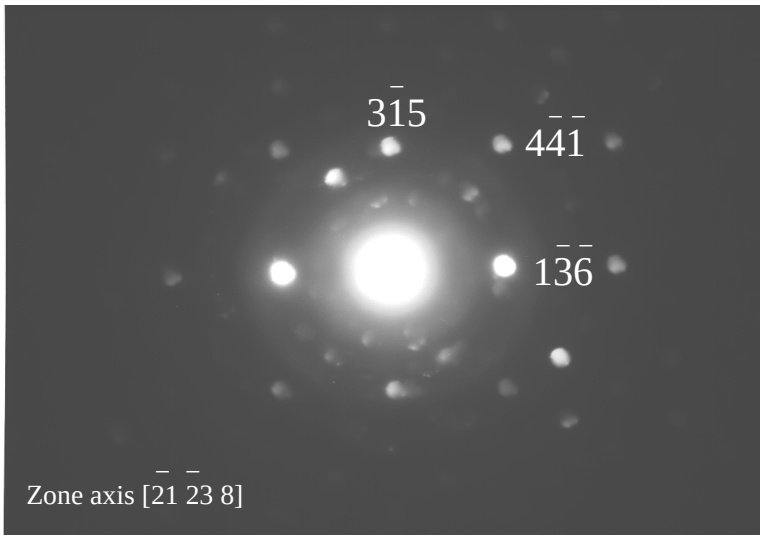

(b)

Figure 7.23: Precipitate M_7C_3 found in HCM2S steel tempered at 600 °C for 3500 h, a) carbon replica b) electron diffraction pattern from M_7C_3.

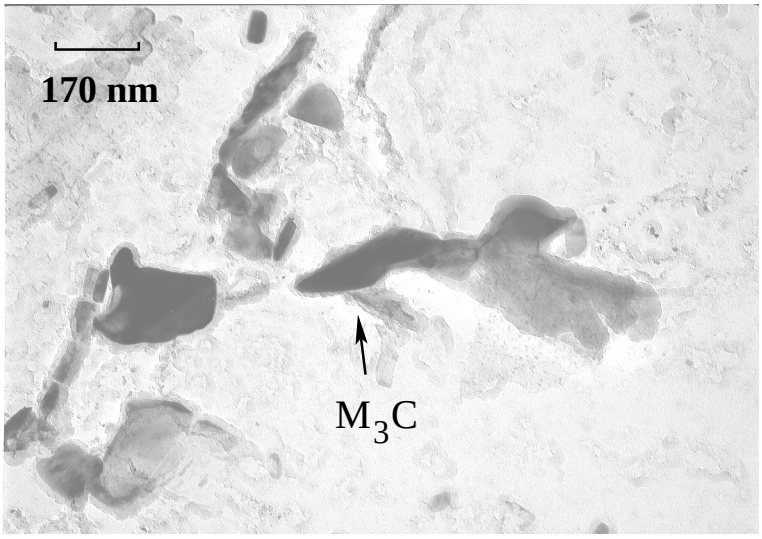

Figure 7.24: Cementite found in new weld metal tempered at 600 °C for 2 h.

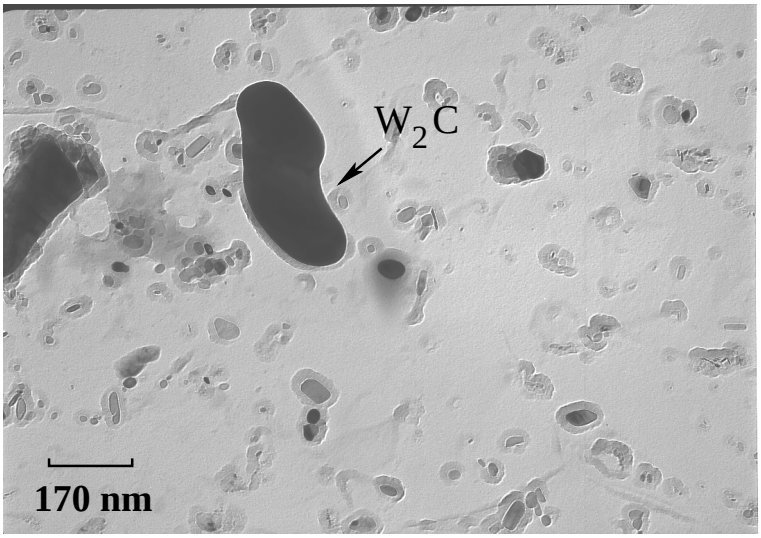

(a)

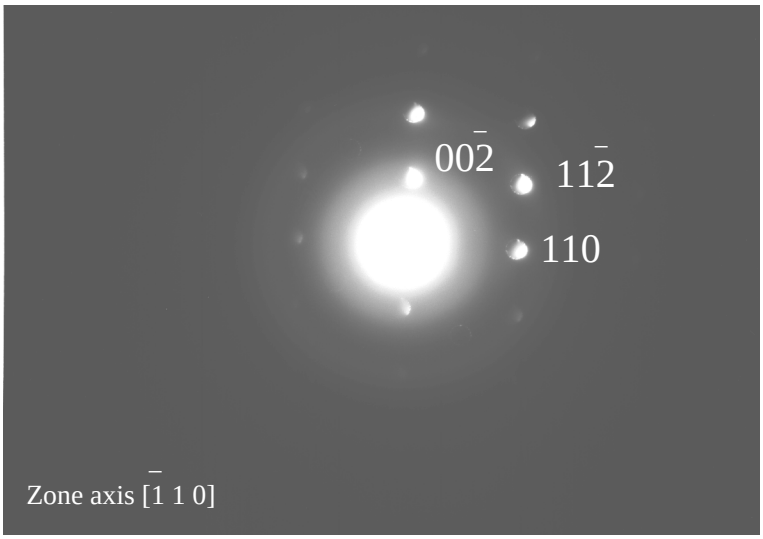

(b)

Figure 7.25: Tungsten carbide (W_2C) found in new weld metal tempered at 600 °C for 3500 h, a) carbon replica b) electron diffraction from W_2C

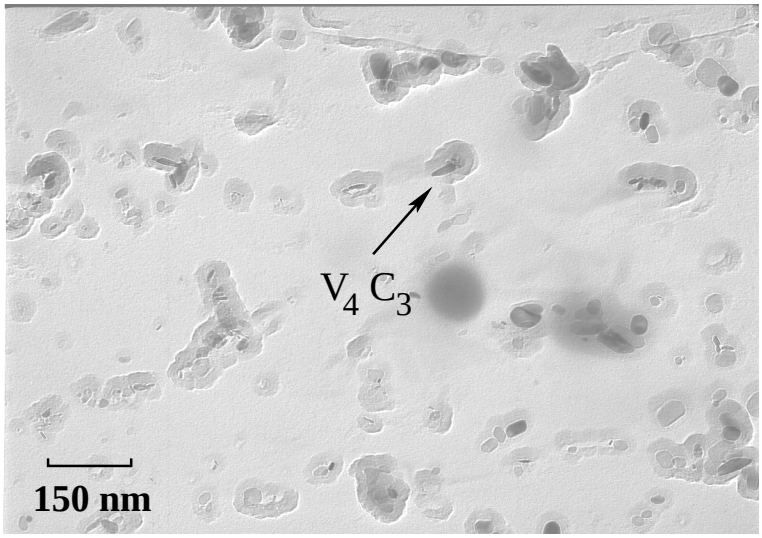

(a)

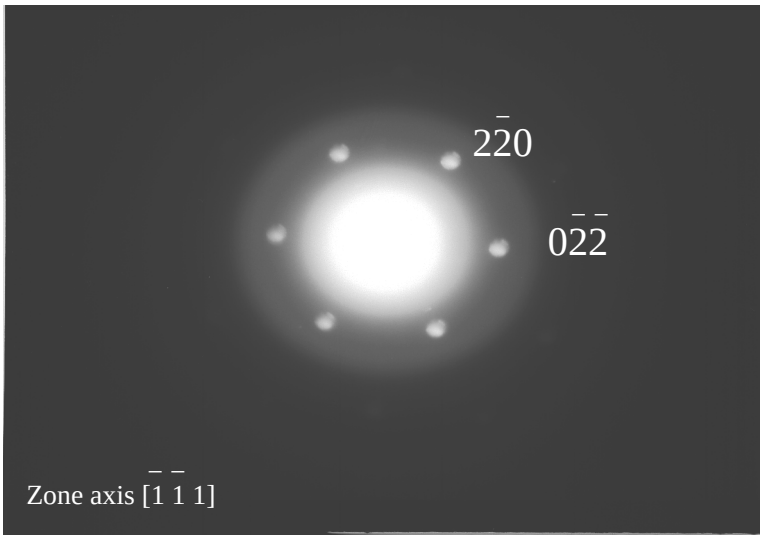

(b)

Figure 7.26: Precipitate V_4C_3 found in new weld metal tempered at 600 °C for 3500 h, a) carbon replica b) electron diffraction pattern from V_4C_3

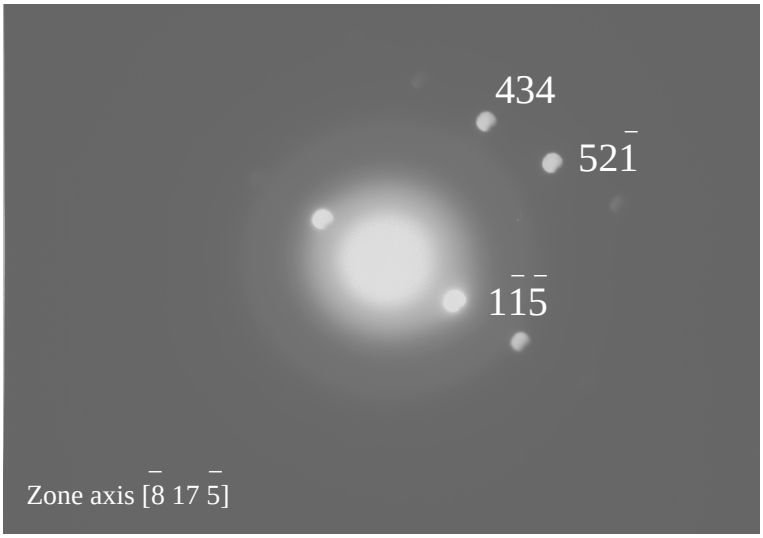

(a)

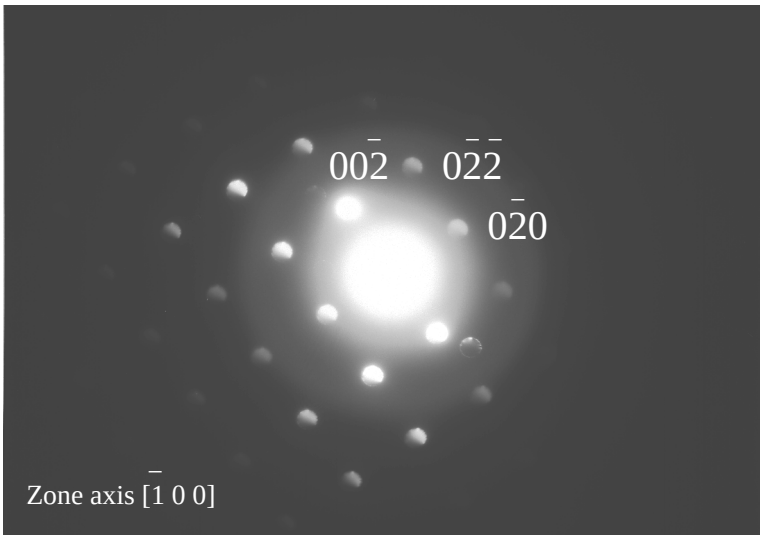

(b)

Figure 7.27: New weld metal tempered at 600 °C for 3500 h, a) electron diffraction pattern from M_7C_3 b) electron diffraction pattern from VC.

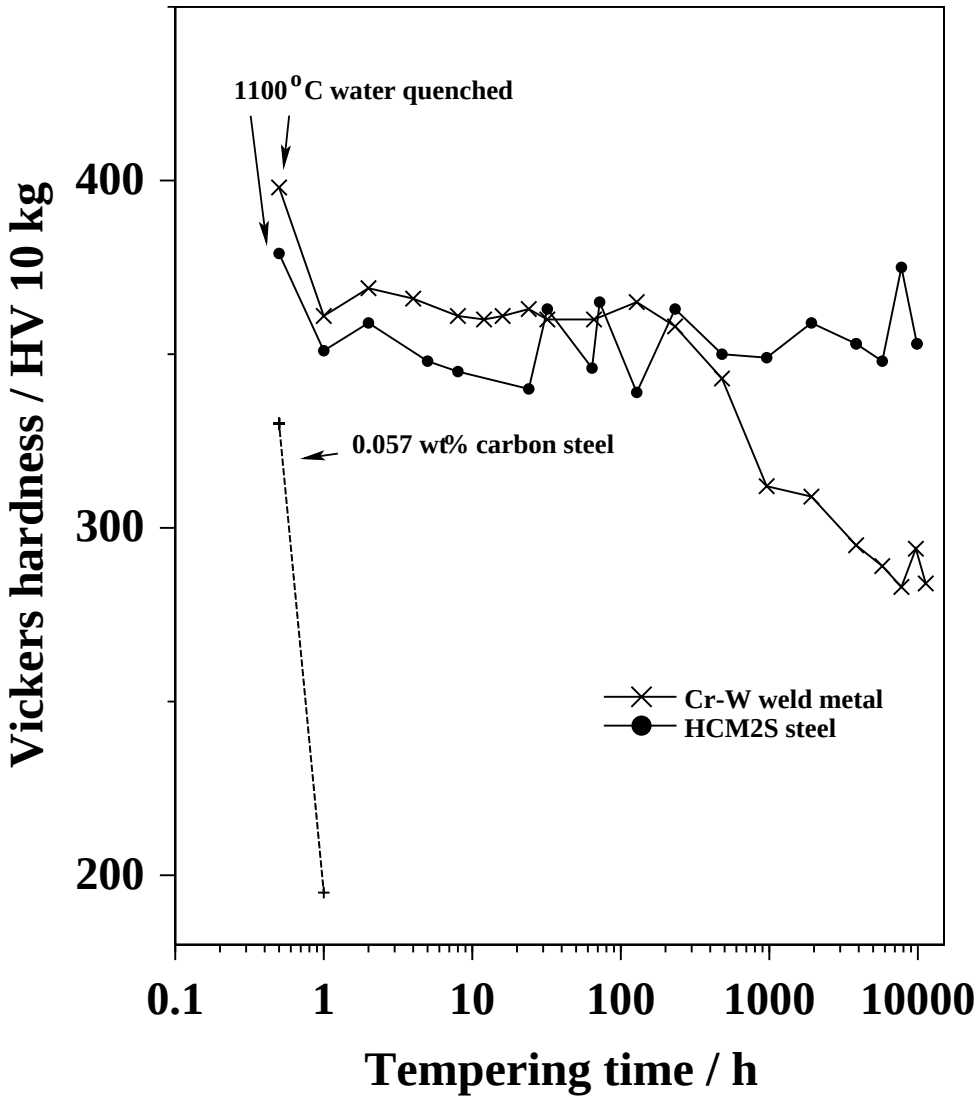

Figure 7.28: Hardness variation in HCM2S steel and Cr–W weld metal tempered at 500 °C.

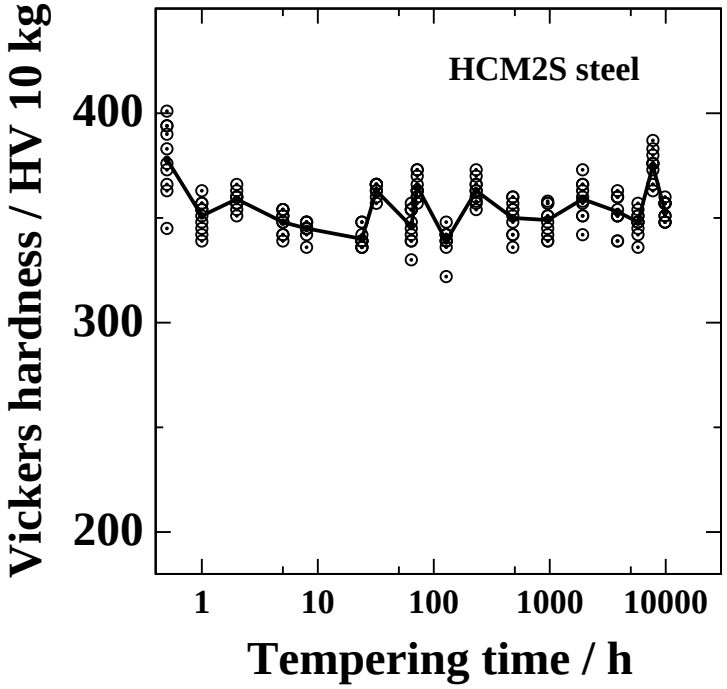

(a)

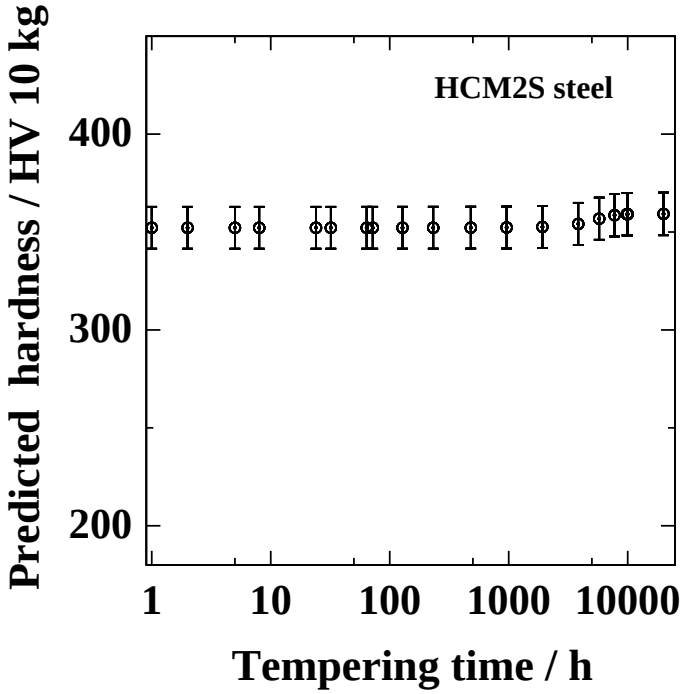

(b)

Figure 7.29: Hardness variation in HCM2S steel tempered at 500 °C, a) measured hardness b) neural network representation of hardness data.

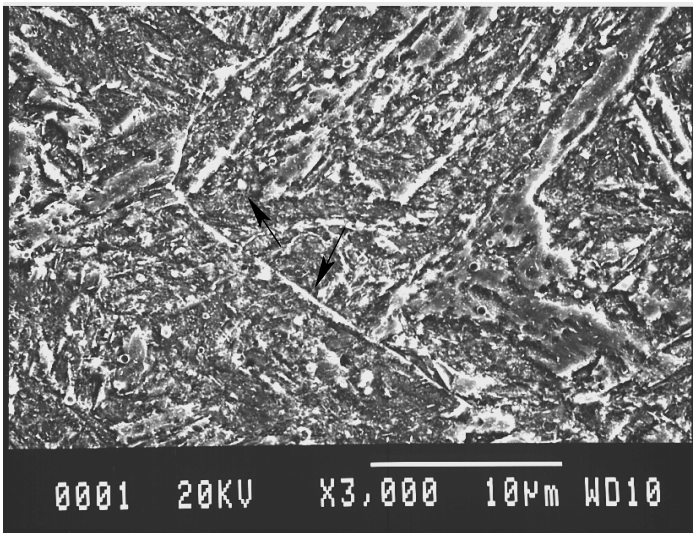

(a)

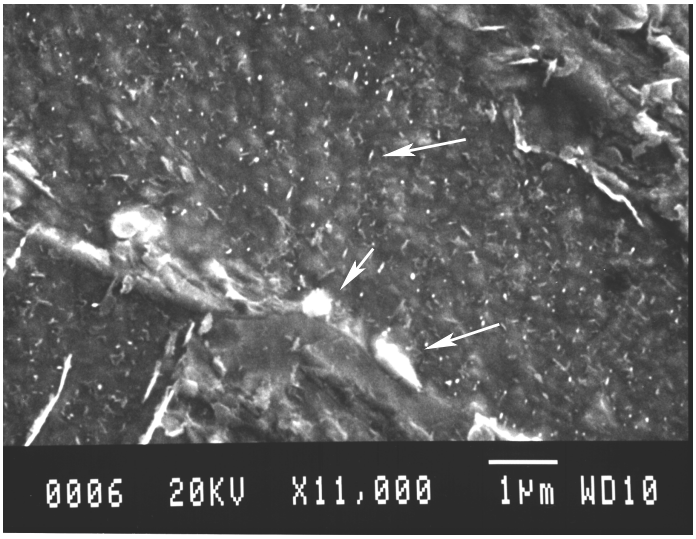

(b)

Figure 7.30: Scanning electron microscopy of HCM2S steel tempered at 500 °C for 10,000 h, a) arrows pointing to precipitates at grain boundary and within the grain b) fine precipitates within grains and coarse precipitates at grain boundaries.

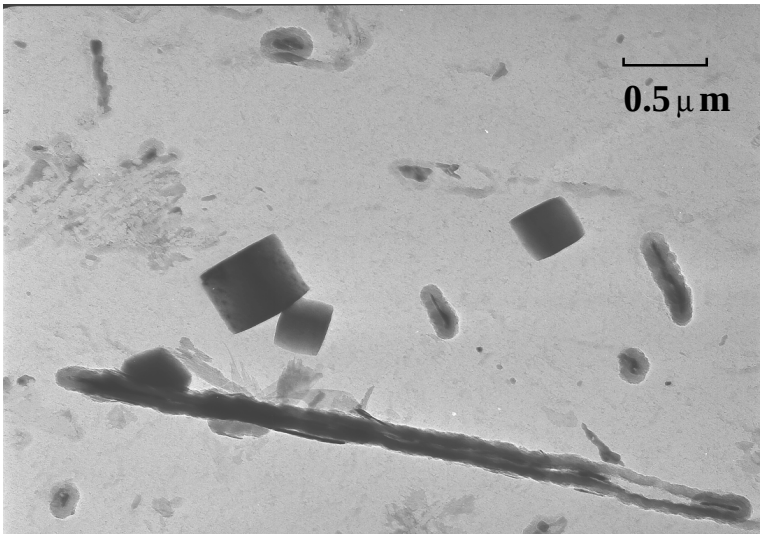

(a)

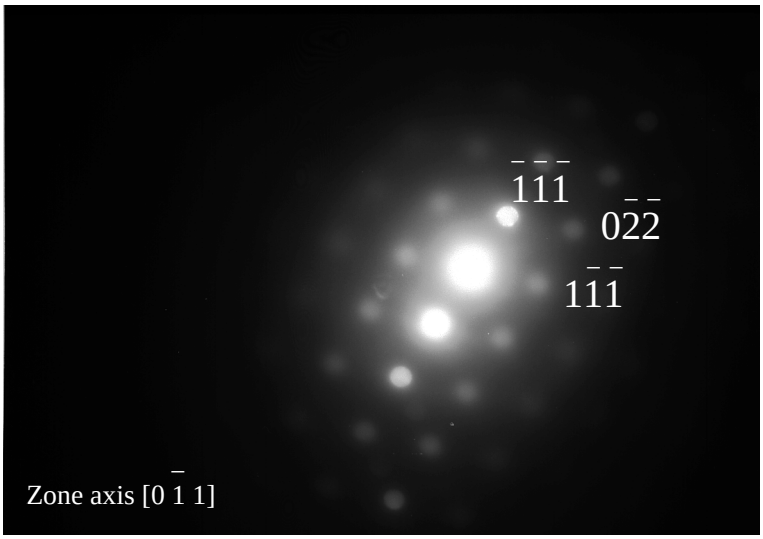

(b)

Figure 7.31: a) Various precipitates found in HCM2S steel tempered at 500 °C for 960 h, a) carbon replica b) electron diffraction pattern from V_4C_3.

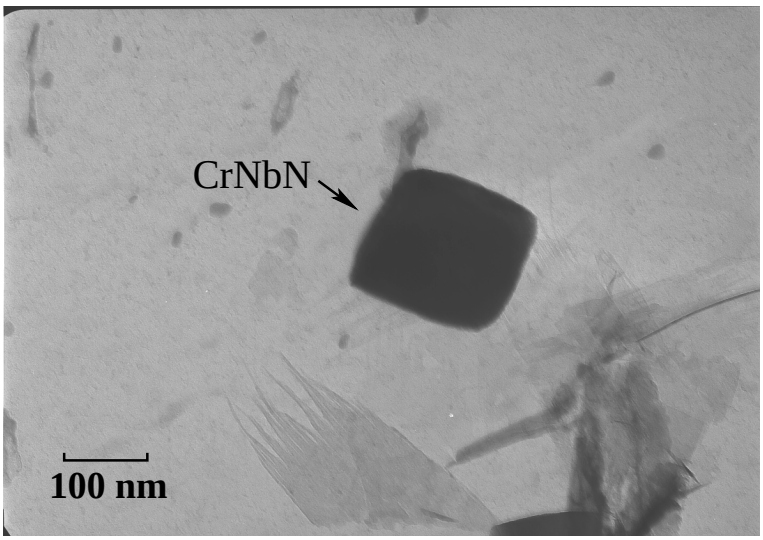

(a)

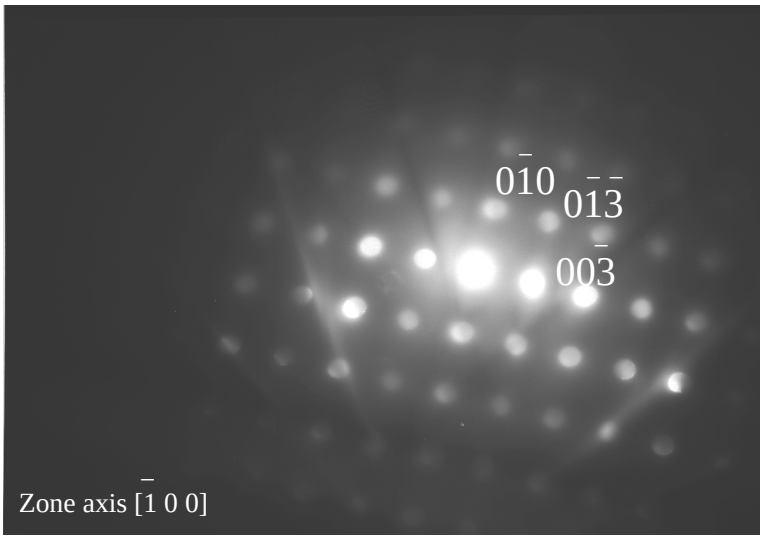

(b)

Figure 7.32: Precipitate CrNbN found in HCM2S steel after tempering at 500 °C for 960 h, a) carbon replica b) electron diffraction pattern from CrNbN.

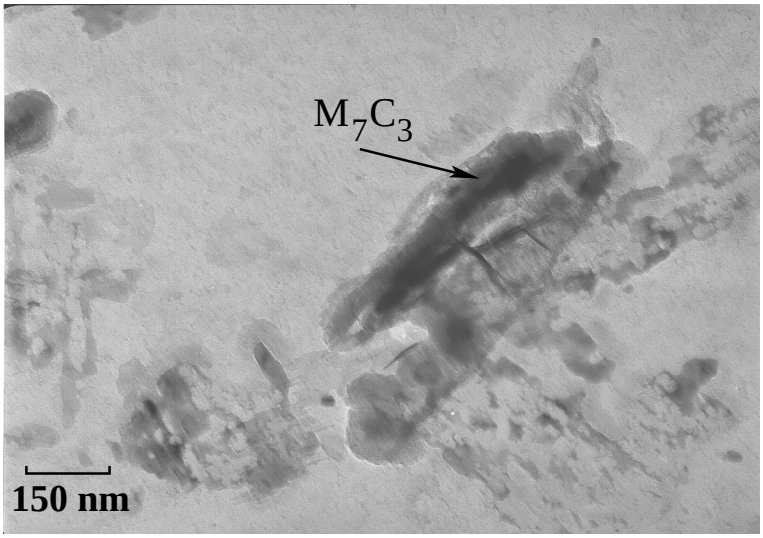

(a)

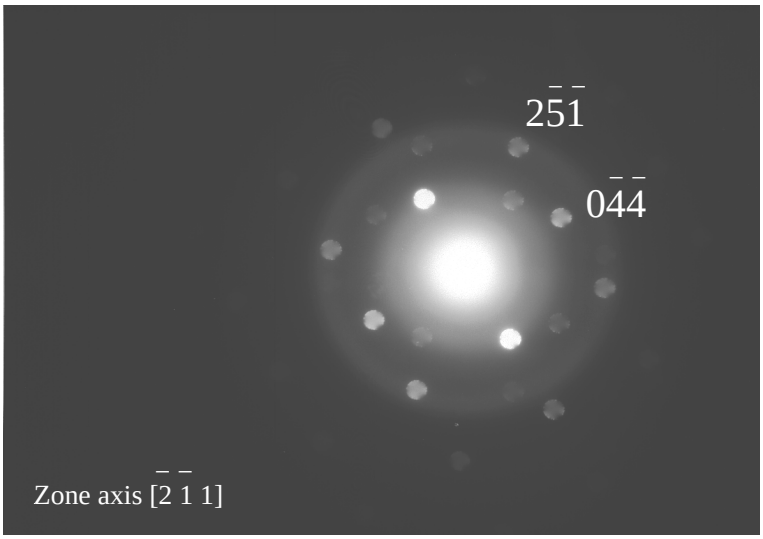

(b)

Figure 7.33: Precipitate M_7C_3 found in HCM2S steel tempered at 500 °C for 960 h, a) carbon replica b) electron diffraction pattern from M_7C_3.

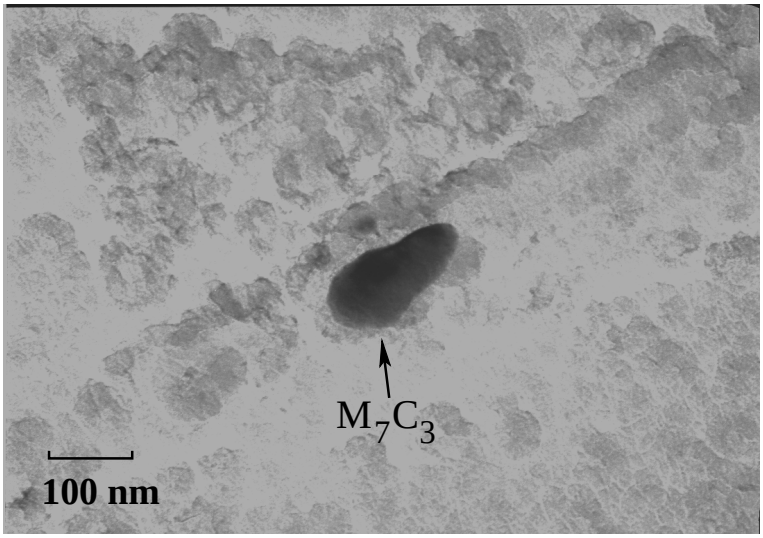

(a)

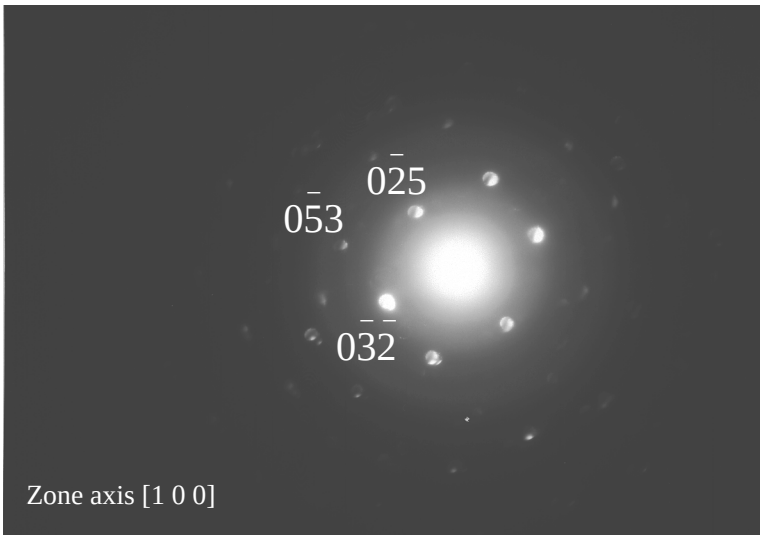

(b)

Figure 7.34: Precipitate M_7C_3 found in HCM2S steel tempered at 500 °C for 10,000 h, a) carbon replica b) electron diffraction pattern from M_7C_3.

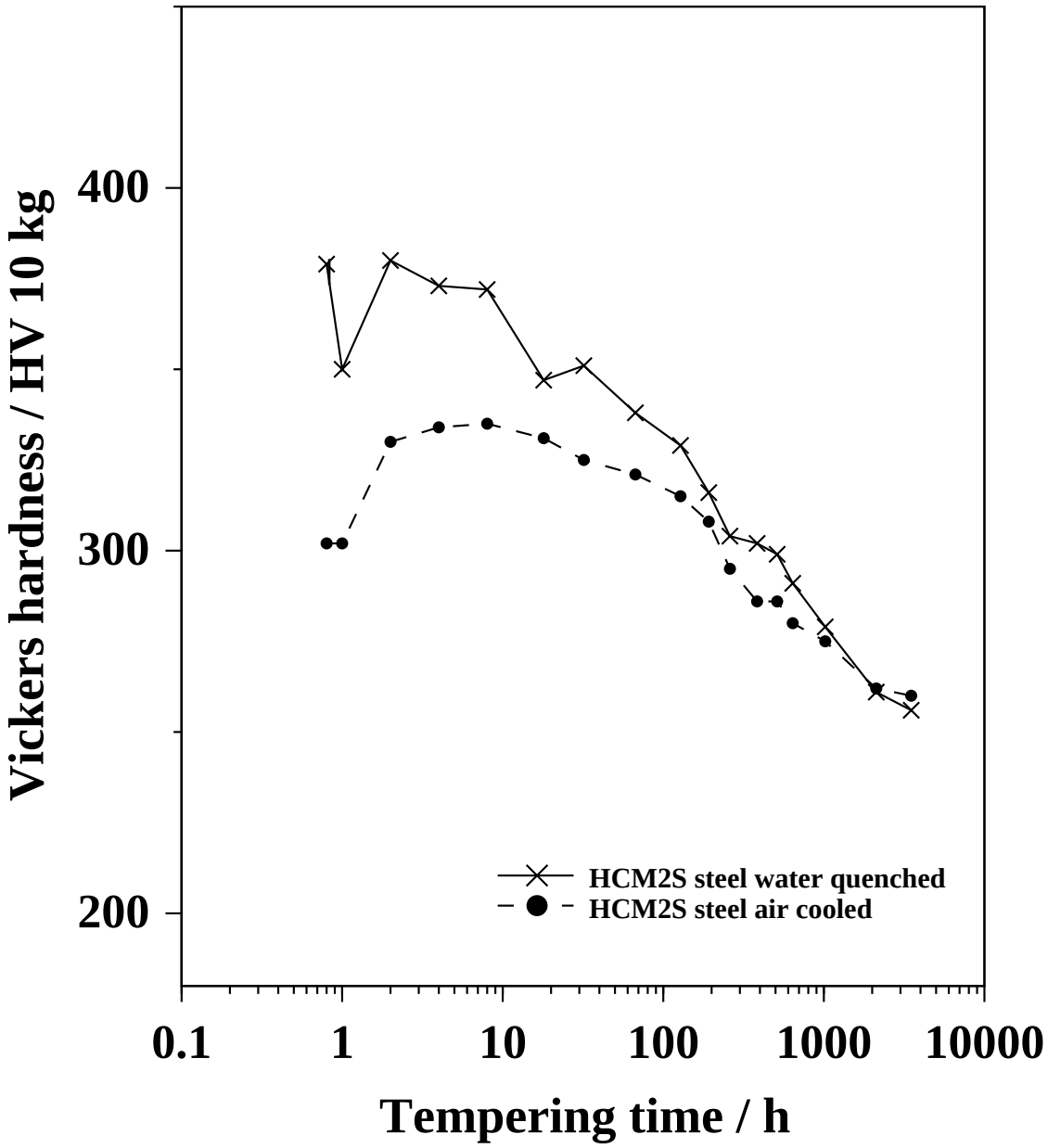

Figure 7.35: Hardness variation in HCM2S steel water quenched and air cooled from 1100 °C and tempered at 600 °C upto 3,500 h.

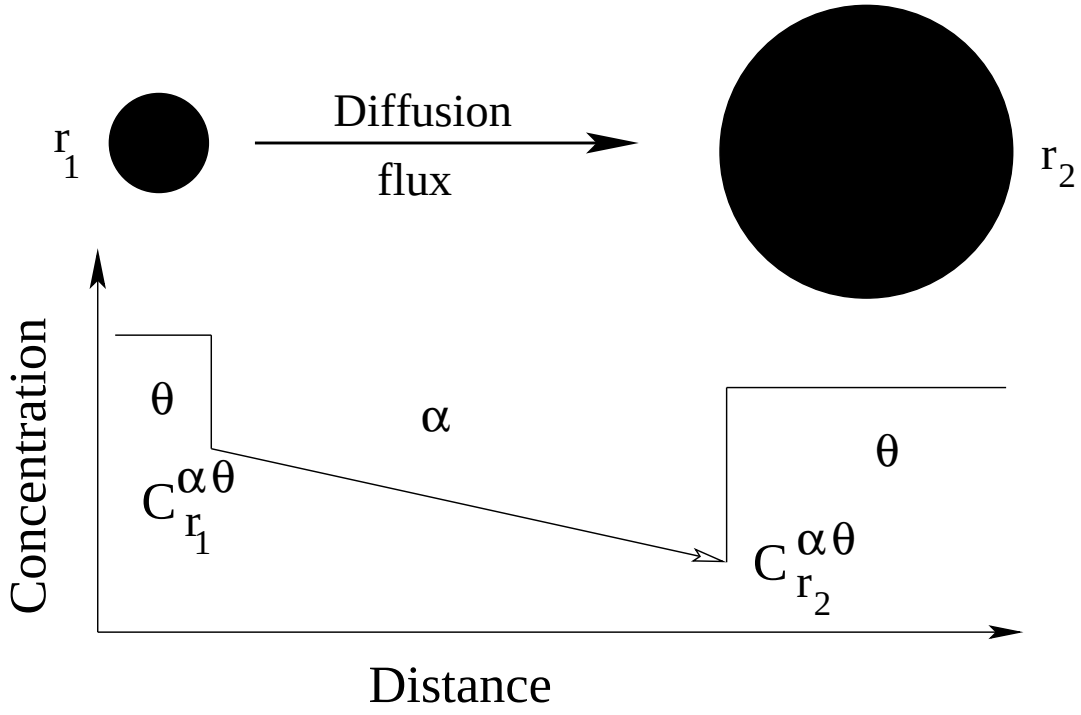

Figure 7.36: Schematic illustration of coarsening of precipitates [142]. α is the matrix, θ is the precipitate, $C^{\alpha\theta}$ is the solute concentration in matrix α and r_1 and r_2 are radii of small and large precipitates respectively.